HAL open science

An onshore bathyal record of tectonics and climate cycles at the onset of the Early-Middle Pleistocene Transition in the eastern Mediterranean

Frédéric Quillévéré, Nadège Nouailhat, Sébastien Joannin, Jean-Jacques Cornee, Pierre Moissette, Christophe Lécuyer, François Fourel, Konstantina Agiadi, Efterpi Koskeridou, Gilles Escarguel

To cite this version:

Frédéric Quillévéré, Nadège Nouailhat, Sébastien Joannin, Jean-Jacques Cornee, Pierre Moissette, et al.. An onshore bathyal record of tectonics and climate cycles at the onset of the Early-Middle Pleistocene Transition in the eastern Mediterranean. Quaternary Science Reviews, 2019, 209, pp.23-39. 10.1016/j.quascirev.2019.02.012 . hal-02060631

HAL Id: hal-02060631

https://univ-lyon1.hal.science/hal-02060631

Submitted on 4 Feb 2021

HAL is a multi-disciplinary open access archive for the deposit and dissemination of scientific research documents, whether they are published or not. The documents may come from teaching and research institutions in France or abroad, or from public or private research centers.

L'archive ouverte pluridisciplinaire **HAL**, est destinée au dépôt et à la diffusion de documents scientifiques de niveau recherche, publiés ou non, émanant des établissements d'enseignement et de recherche français ou étrangers, des laboratoires publics ou privés.

Distributed under a Creative Commons Attribution - NoDerivatives 4.0 International License

Version of Record: https://www.sciencedirect.com/science/article/pii/S0277379118305924
Manuscript_a282f57521aa34e02c8391302197c76b

An onshore bathyal record of tectonics and climate cycles at the onset of the Early-Middle Pleistocene Transition in the eastern Mediterranean

Frédéric Quillévéré[a#], Nadège Nouailhat[a], Sébastien Joannin[b], Jean-Jacques Cornée[c], Pierre Moissette[d], Christophe Lécuyer[a], François Fourel[e], Konstantina Agiadi[d], Efterpi Koskeridou[d], Gilles Escarguel[e]

[a] Univ. Lyon, Université Claude Bernard Lyon 1, ENS de Lyon, CNRS, UMR 5276 LGL-TPE, F-69622 Villeurbanne, France

[b] CNRS UMR 5554, Institut des Sciences de l'Evolution de Montpellier, Université de Montpellier, Montpellier, France

[c] UMR 5243 CNRS, Geosciences Montpellier, Université de Montpellier, Université des Antilles, Pointe-à-Pitre (FWI), France

[d] Department of Historical Geology and Palaeontology, Faculty of Geology and Geoenvironment, University of Athens, Panepistimioupolis 15784, Athens, Greece

[e] Univ. Lyon, Laboratoire d'Ecologie des Hydrosystèmes Naturels et Anthropisés, UMR 5023 LEHNA, CNRS, ENTPE, Université Lyon 1, F-69622 Villeurbanne, France

[#] Corresponding author. E-mail address: frederic.quillevere@univ-lyon1.fr

© 2019 published by Elsevier. This manuscript is made available under the Elsevier user license
https://www.elsevier.com/open-access/userlicense/1.0/

Abstract

Early Pleistocene (Calabrian) clays of the Lindos Bay Formation have been uplifted and are exposed today on the eastern coast of Rhodes (Hellenic forearc, Greece). The hemipelagic origin of these sediments and the excellent preservation of the microfossils they contain, make the Lindos Bay Formation a unique element in the eastern Mediterranean, which has the potential to constitute a paleoclimate referential framework of the region for the Early-Middle Pleistocene Transition (EMPT). In this context, 98 samples were collected in the type locality section of the Lindos Bay Formation. Stable isotope ($\delta^{18}O$, $\delta^{13}C$) analyses were carried out on benthic (*Uvigerina peregrina*) and planktonic (*Globigerina bulloides*) foraminifera for the interval between ~1100 ka and ~858 ka. We identify and continuously reconstruct the climate cycles that occurred between Marine Isotope Stages (MIS) 32 and 21. Counts of planktonic foraminifera were further carried out and allow connecting the conditions occurring locally in the surface waters with the glacial-interglacial cycles during the onset of the EMPT. While (sub)tropical taxa dominate the assemblages, glacials were associated with short-term (<~10 kyr) influxes of temperate to subpolar species suggesting cooling and/or increasing productivity in the surface waters correlating with the deposition of sapropels in the eastern Mediterranean deep sea. Finally, planktonic/benthic foraminiferal ratios show that the section deposited at upper bathyal depths between ~450 m and ~150 m. During the late Early Pleistocene, the eastern coast of Rhodes has locally undergone repeated, transient and possibly very rapid vertical motions which are overprinted on a regional tectonically-forced regressive trend.

Keywords: Stable isotopes; Micropaleontology, Foraminifers; Paleoclimatology; Climate cycles; Neotectonics; Pleistocene; Eastern Mediterranean

1. Introduction

The Dodecanese island of Rhodes (Greece) is renowned for its particularly well exposed, easily accessible, and very fossiliferous Pleistocene marine deposits (e.g., Meulenkamp et al., 1972; Moissette and Spjeldnaes, 1995; Hanken et al., 1996; Hansen, 1999; Kovacs and Spjeldnaes, 1999; Titschack and Freiwald, 2005; Titschack et al., 2005; 2008; Steinthorsdottir et al., 2006; Joannin et al., 2007a; Moissette et al., 2007; 2013; 2016; Lécuyer et al., 2012; Steinthorsdottir and Hakansson, 2017; Agiadi et al., 2018; Cornée et al., 2019). Rhodes is located in the easternmost part of the Hellenic sedimentary forearc (Fig. 1A, B). Since the Pliocene, because of the increasing curvature of the African/Eurasian plate boundary, the eastern part of the forearc suffered severe stretching accommodated along N70° trending strike-slip faults parallel to the plate boundary, anticlockwise rotation and vertical motions (e.g., Duermeijer et al., 2000; Ten Veen and Kleinspehn, 2002; Van Hinsbergen et al., 2007), concomitant with the opening of the >4000 m deep marine Rhodes Basin (Fig. 1B) to the east of the island (Woodside et al., 2000; Hall et al., 2009). Rhodes experienced important tectonic changes coeval with the opening of the Rhodes Basin. Tectonics during the Early and Middle Pleistocene resulted in drowning and uplift related to alternating southeastward-northwestward tiltings (Hanken et al., 1996; van Hinsbergen et al., 2007). These vertical motions are responsible for the major, long-term transgression-regression cycle that first promoted deposition and then emergence of deep marine sedimentary sequences, which are today exposed onshore in patchily preserved grabens or micro-basins along the eastern coast of Rhodes (Fig. 1C).

The sedimentary succession resulting from this tectonically-driven cycle has been qualified as the Rhodes Synthem (Fig. 2; Hanken et al., 1996; Cornée et al., 2006a; 2019; Titschack et al., 2013). Deposition of this lithostratigraphic unit started during the late Gelasian (Moissette et al., 2016) with the shallow marine siliciclastic deposits and bioclastic

limestones of the Kolymbia Formation. It ended during the Ionian (Titschack et al., 2013; Cornée et al., 2019) with the shallow marine pluri-facies limestones or siliciclastic deposits of the Cape Arkhangelos Formation. Within the Rhodes Synthem, between the Kolymbia Formation and the Cape Arkhangelos Formation (Fig. 2), the blue-grey calcareous to silty clays of the Lindos Bay Formation (and the associated limestones of the Saint Paul's Bay Formation) constitute the most pronounced tectonic drowning of the island. Previous studies of the Lindos Bay Formation have shown that these clays deposited in a hemipelagic setting, at bathyal depths during the interval of maximum transgression during the Calabrian (Moissette and Spjeldnaes, 1995; Hanken et al., 1996; Kovacs and Spjeldnaes, 1999; Rasmussen and Thomsen, 2005; Van Hinsbergen et al., 2007; Quillévéré et al., 2016; Milker et al., 2017). Such Pleistocene deep-water deposits accessible on land have revealed unique for the eastern Mediterranean. Indeed, it has been possible to achieve calcareous plankton biostratigraphic and/or magnetostratigraphic analyses of these deposits because of their hemipelagic origin (Løvlie et al., 1989; Thomsen et al., 2001; Cornée et al., 2006a; 2006b; Titschack et al., 2013; Quillévéré et al., 2016). These analyses have thus made the Lindos Bay Formation an anchor point to resolve the chronostratigraphy of the Early to Middle Pleistocene of Rhodes and a key target to quantify the vertical motions undergone by the island during this time. They have further suggested that the Lindos Bay Formation may serve as a useful archive for reconstructing the environmental changes that occurred in the eastern Mediterranean when the global climate underwent a transition from relatively warm conditions during the Early Pleistocene to the substantially cooler regime of the Middle Pleistocene.

The different exposures of the Lindos Bay Formation along the eastern coast of Rhodes are highly diachronous, as a result of deposition in independent steep and irregular micro-basins developed at different elevations (Hanken et al., 1996; Titschack et al., 2013;

Quillévéré et al., 2016). In a recent chronostratigraphic survey of these exposures, Quillévéré et al. (2016) showed that the northern Lindos Bay section (Fig. 1D), which is the focus of this study, exhibits the thickest and most continuous record for the late Early Pleistocene (late Calabrian) interval. During this interval, Earth's climate initiated important changes when the amplitude and duration of climate oscillations progressively increased, leading to the spread of ice volumes in the northern hemisphere during glacials. The late Calabrian was then marked by an increasing asymmetry of the glacial-interglacial cycles which finally led to a shift from 41-kyr to 100-kyr orbital rhythm during the so-called Early-Middle Pleistocene Transition (EMPT; e.g., Ruddiman et al., 1989; Lisieki and Raymo, 2005; 2007; Head and Gibbard, 2015), which occurred between 1200 ka and 600 ka (Clark et al., 2006). In the Mediterranean region, late Calabrian records and associated climate changes have been documented onshore in other uplifted hemipelagic sections, but only in its central part at coastlines of the Ionian Sea (e.g., Rio et al., 1996; Joannin et al., 2007b; Ciaranfi et al., 2010; Papanikolaou et al., 2011; Colleoni et al., 2012; Capraro et al., 2017). The availability of hemipelagic clays in the northern Lindos Bay section thus provides the first opportunity for studying, at high resolution, such a comparable onshore record in the eastern part of the Mediterranean region.

The present study consequently aims to provide a late Calabrian record of climate variations for the eastern Mediterranean region in a controlled depositional setting. Based on the analysis of the oxygen ($\delta^{18}O$) and carbon ($\delta^{13}C$) isotope compositions of benthic and planktonic foraminifera, we reconstruct and identify the climate cycles recorded in the northern Lindos Bay section. Counts of planktonic foraminifera are carried out to connect the environnmental conditions occurring in the surface waters with the identified glacial-interglacial cycles. Conducting these counts, we take the opportunity to also use the variation

in planktonic/benthic foraminiferal ratios to estimate the depth changes related to vertical motions that occurred during deposition.

2. The northern Lindos Bay section

The Lindos Bay (36°5'57"N; 28°5'12"E) is located ~2 km north of the village of Lindos. It exhibits two sedimentary exposures separated by ~200 m (southern outcrop and northern outcrop in Quillévéré et al. [2016]), which together constitute the thickest (~45 m) record of the Lindos Bay Formation. Here, we study the northern exposure, which constitutes the type locality for the Lindos Bay Formation (Hanken et al., 1996). The section crops out just above present-day sea level at the north side of the Lindos Bay (Fig. 1D). It consists of 27 meters of massive and homogenous blue-grey clays. Very fossiliferous, the clays yield a diversified bathyal fauna including benthic foraminifera, ostracods, scaphopods, bivalves, brachiopods, bryozoans, echinoids, fish otoliths and trace fossils (*Zoophycos*) (Moissette and Spjeldnaes, 1995; Hanken et al., 1996). They also exhibit abundant and diversified calcareous planktonic organisms (Quillévéré et al., 2016) including nannofossils, planktonic foraminifera and pteropods, whose aragonite shells are still preserved. Based on a stratigraphically low-resolution (13 samples) analysis of bryozoan assemblages, Moissette and Spjeldnaes (1995) estimated that the clays deposited at upper bathyal depths between 200 m and 400 m. Biostratigraphic and magnetostratigraphic analyses by Quillévéré et al. (2016) further showed that hemipelagic deposition occurred continuously during the late Calabrian from the late part of Chron C1r.2r to the late part of Chron C1r.1 (Matuyama), spanning calcareous nannofossil Zones CNPL9 and CNPL10 of Backman et al. (2012) (Fig. 1E). The northern section in the Lindos Bay thus covers the upper part of the Lindos Bay Formation. It is unconformably overlain by the shallow water calcarenite of the Cape Arkhangelos Formation representing the

shallowing upward trend of the Rhodes Synthem (Hanken et al., 1996; Hansen, 1999; Titschack et al., 2013).

3. Material and methods

3.1. Sampling

The 27 m-thick northern section of the Lindos Bay was sampled in June 2015. The present work is based on the analysis of 98 samples of ~3 cm thickness collected every ~25-28 cm (Fig. 1E). All samples were dug into the steep ground (Fig. 1D) for a burial depth of ~20-30 cm to minimise the potential effects of present-day erosion and weathering. All 98 samples were washed over a 63 µm screen and the residue was dry-sieved.

3.2. Oxygen and carbon isotope analyses

Bottom and surface water oxygen and carbon isotope compositions ($\delta^{18}O$, $\delta^{13}C$) were measured from the 98 sediment samples on the benthic foraminifera *Uvigerina peregrina* and the planktonic foraminifera *Globigerina bulloides,* respectively. Both taxa occur continuously throughout the section. *Uvigerina* spp. are shallow infaunal benthic foraminifera whose $\delta^{18}O$ values constitute a powerful practical tool for global scale correlation, since they represent a strong glacio-eustatic component during the time interval considered in this study (e.g., Elderfield et al., 2012). *Globigerina bulloides* is an algal symbiont-barren species of planktonic foraminifera, whose symbiont effects on the stable isotope compositions can be excluded. In the Mediterranean, it calcifies primarily during the spring bloom (Pujol and Vergnaud Grazzini, 1995), mainly at intermediate depths of the photic zone in stratified water masses (Schiebel and Hemleben, 2017). It is consequently less affected by changes in regional fresh-water dilution than other shallow-dwelling species of planktonic foraminifera.

All measurements were performed using specimens hand-picked from the size-fraction 250-355 µm. About 15 specimens of *G. bulloides* and 10 specimens of *U. peregrina* were necessary to supply sufficient calcium carbonate and to limit the effect of individual variation on the isotopic values (e.g., Fourel et al., 2015). The specimens analyzed were free of carbonate infilling or visible dissolution features. Careful observation of the shell ultrastructure of randomly selected specimens at high magnification (×2000) using a Zeiss Merlin SEM confirmed the excellent preservation of the foraminifera (Fig. 3). They were further utrasonically cleaned in distilled water, and weighted prior to isotope ratio analyses. Oxygen and carbon isotope ratio measurements were performed with an Elementar MultiPrep system on line with a dual Inlet IsoPrime™ Isotope Ratio Mass Spectrometer (IRMS). The principle of the fully automated device is to react the calcium carbonates with anhydrous phosphoric acid at 90°C to generate CO_2, which is then analyzed with the mass spectrometer. The full process is described in Fourel et al. (2015). Most samples were analyzed through the dual inlet variable volumes but some of them, when sample amounts were too small, had to be analyzed using the dual inlet cold finger. Isotopic compositions were quoted in the standard δ-notation in ‰ relative to V-PDB for both $^{18}O/^{16}O$ and $^{13}C/^{12}C$. Repeated analysis of an in-house Carrara Marble standard calibrated against international references NBS 19, NBS 18, and IAEA-CO-8, suggested that repeatabilities for $\delta^{18}O$ and $\delta^{13}C$ measurements were 0.05‰ and 0.09‰, respectively. Replicate analyses of 9 benthic and planktonic foraminiferal samples generated replicate data within the repeatability of the method for both $\delta^{18}O$ and $\delta^{13}C$ (Table 1).

Time series analyses of both *G. bulloides* and *U. peregrina* oxygen isotope data-sets were performed using the PAST 3.22 software (Hammer et al., 2001) in order to test for statistically significant cyclicity related to orbital parameters. Spectral analyses were conducted with a REDFIT module (Schulz and Mudelsee, 2002) with a Blackman-Harris

window. They are presented with the 80%, 90% and 95% confidence intervals. Wavelet analyses for unequally spaced samples were also performed. Resulting scalograms allow vizualizing potential cyclicity changes in strength and frequency through time.

3.3. Planktonic foraminiferal counts and statistical treatments

Planktonic foraminiferal counts were carried out on all 98 samples. In each residue, the size fraction coarser than 125 µm was homogenized and split with a microsplitter into representative aliquots. One of the last two splits was distributed on a gridded tray. Quantitative data of 20 taxa and morphotypes (see below) frequencies were obtained by counting 300 specimens per aliquot. All representative specimens were identified following the taxonomic concepts and nomenclature of Kennett and Srinivasan (1983) and their raw counts were transformed into percentages over the total abundance of planktonic foraminifera. *Globigerina bulloides* and *Globigerina falconensis* were counted together under the name *G. bulloides* because of their close similarity and identical ecological requirements. Furthermore, dextral and sinistral morphotypes of *Neogloboquadrina pachyderma*, *Globorotalia truncatulinoides* and *Globorotalia crassaformis* were counted separatly based on the right- or left-coiled direction of their shell. Finally, specimens of *Trilobatus sacculifer* (*sensu* André et al., 2013) were divided into two morphotypes depending on whether or not they harbored an elongate «sac-like» final chamber. All broken and/or non-identified shells of planktonic foraminifera were classified into a unique category without taxonomic attribution.

In order to quantitatively describe the planktonic foraminiferal assemblages succession in the Lindos Bay section, the raw abundance data of the 20 taxa and morphotypes found there were subjected to statistical treatments with PAST 3.22. First, stratigraphically constrained Q-mode hierarchical Cluster Analysis (hCA) was computed with the paired group (UPGMA) algorithm based on a Bray-Curtis similarity matrix. The hCA identifies nested and successive

clusters of planktonic foraminiferal assemblages under a stratigraphic ordering constraint. These clusters were then tested for significance against the null hypothesis of random compositional differences using overall and pairwise ANOSIM tests based on the same Bray-Curtis similarity matrix. Second, Correspondence Analysis (CA) based on taxa/morphotype raw counts was performed on the 98 samples in order to assign a probable ecological habitat to the previously identified clusters of planktonic foraminiferal assemblages. More specifically, the CA results were used to qualitatively connect the previously documented significant clusters of planktonic foraminifera with surface water temperature trends, distinguishing between «warmer» and «cooler» assemblages.

3.4. Paleodepth estimates

To estimate the depositional depth of the sediments in the northern Lindos Bay section, planktonic/benthic ratios (*sensu* Gibson, 1989) were determined by counting the number of planktonic foraminifera relative to the total number of foraminifera (counted up to 300 planktonic specimens) in all 98 samples. The planktonic/benthic ratio (P/P+B) classicaly increases with water depth and distance from shorelines, to reach a value of ~1 in lower bathyal (*sensu* Emig, 1997) environments (e.g., Berger and Diester-Haas, 1988). P/P+B ratios were consequently measured in all 98 samples and the values were associated with an estimated paleodepth following the model of Gibson (1989). They were further corrected from the effect of relative, glacio-eustatic sea-level changes as compared with the current sea level at Gibraltar. This was achieved by using the equations of Rohling et al. (2014), which were used to convert Mediterranean foraminiferal $\delta^{18}O$ values to Relative Sea Levels at Gibraltar.

4. Results

4.1.Stable isotope compositions

The $\delta^{18}O$ values of *Globigerina bulloides* and *Uvigerina peregrina* vary between -0.1‰ and 2.5‰, and between 1‰ and 3.4‰, respectively (Table 1, Fig. 4). They exhibit an average gradient of 1.2‰ between surface and bottom waters and show similar overall variation trends throughout the section.

The $\delta^{13}C$ values of *G. bulloides* and *U. peregrina* vary between -2.5‰ and 0.9‰, and between -2.1‰ and 0.6‰, respectively (Table 1, Fig. 4). Lower values are recorded in the upper part of the section above ~15 m. The $\delta^{13}C$ record exhibits a weak vertical gradient between planktonic and benthic foraminifera throughout the section.

4.2. Planktonic foraminiferal counts and statistical treatments

Counts of planktonic foraminiferal taxa/morphotypes are provided in the Supplementary Table S1. Planktonic foraminifera are abundant, remarkably well preserved (Fig. 3) and the assemblages are well diversified (20 taxa and morphotypes) in all 98 samples. None of the 98 samples exhibits evidence of carbonate dissolution nor significant fragmentation of the foraminiferal shells. *Globigerinoides ruber* is by far the most abundant taxon (Fig. 5A). It shows repeated abundance fluctuations throughout the section, reaching up to 80% maximum values in some intervals. Other dominant species and morphotypes include *Globigerina bulloides*, dextral and sinistral *Neogloboquadrina pachyderma*, *Orbulina* sp. and *Globigerinella siphonifera*, which all occur nearly continuously with fluctuating abundances reaching maximum values of 36%, 35%, 26%, 25%, and 6%, respectively. *Globorotalia inflata* and *Trilobatus sacculifer* occur discontinuously but reach significant abundance values (up to 42% and 12%, respectively) in certain intervals. The increasing abundances of the (sub)tropical morphospecies *Gs. ruber* are globally correlated with the decreasing abundances of the temperate to subpolar morphospecies/morphotypes *Gr. inflata*, dextral *N. pachyderma*,

and sinistral *N. pachyderma*. The abundance of the cosmopolitan morphospecies *G. bulloides* closely parallels changes in the abundance of dextral and sinistral *N. pachyderma*.

The hierarchical Cluster Analysis (hCA) reveals the presence of 17 distinct, statistically significant and stratigraphically controlled clusters of assemblages throughout the section (Fig. 5A, B). The results of the Correspondence Analysis (CA) applied to the assemblages data-set (Fig. 6) indicate that positive scores on the first axis (28% of the total variation) are associated with tropical to subtropical morphospecies, including *Gs. ruber, Globigerinoides conglobatus, T. sacculifer, Sphaeroidinella dehiscens* and *Beella digitata*, which all favor warm surface waters (Schiebel and Hemleben, 2017). On the contrary, negative scores are mostly carried either by ubiquitous (*Turborotalia quinqueloba*, *Globigerinita glutinata*), or subtropical to temperate (*Orbulina* sp., *Ge. siphonifera*), temperate to subpolar (dextral *N. pachyderma*, *G. bulloides*, *Gr. inflata*, *Globorotalia scitula*, *Globigerinita uvula*) or even subpolar to polar (sinistral *N. pachyderma*) taxa, which globally favor cooler and/or more nutritive surface waters (Schiebel and Hemleben, 2017). Based on the scores on the first axis of the CA (Fig. 5C), we consequently assigned a probable habitat for the significantly different clusters of planktonic foraminiferal assemblages identified after the hCA, distinguishing a succession of 7 «cooler» (CA-1 < 0) and 7 «warmer» (CA-1 > 0) intervals in the northern Lindos Bay section (Fig. 5A).

4.3. Paleodepths

Planktonic foraminifera are constantly far more abundant than benthic foraminifera (Supplementary Table S1). Planktonic/benthic ratios show variations throughout the section, with P/P+B values ranging between 0.58 and 0.94 (Fig. 5D; Table 1). Among the 98 analyzed samples and following Murray (1991), 83 were apparently deposited in the upper bathyal zone (P/P+B > 0.70) and 15 in the outer shelf zone (0.50 ≤ P/P+B/ ≤ 0.70). Application of the

Gibson (1989) regression suggests that deposition of the Lindos bay section occurred between ~129 m and ~445 m below sea level, these paleodepths being refined to ~138 m and ~497 m (Fig. 5E) when corrected from the effect of glacio-eustatic sea-level changes. Highest depth values are reached in the middle part of the section between ~12 m and ~13.5 m and lower depth values are reached in the uppermost part of the section. We note in addition that P/P+B ratios and paleodepth estimates show more fluctuating values in the lower part of the section (below 15 m) than in its upper part (above 15 m), with in particular three intervals of apparent deepening and shallowing recorded between 3 m and 15 m.

5. Discussion

5.1. Re-examination of the age model and estimated sedimentation rates

Based on the magnetostratigraphic and calcareous nannofossil biostratigraphic data available from Quillévéré et al. (2016), we built an age model using the Global Polarity Time Scale (GPTS) of Lourens et al. (2005) and estimated the sedimentation rates through the northern Lindos Bay section (Fig. 7). Our age model relies on tie points corresponding to the lowest common occurrence of *Reticulofenestra asanoi* (1078 ka) at 1.95 m, the C1r.2r/C1r.1n (Jaramillo) reversal (1072 ka) at 2.23 m, the C1r.1n (Jaramillo)/C1r.1r (Matuyama) reversal (988 ka) at 9.46 m, the reentrance datum of medium *Gephyrocapsa* (956-985 ka) at 9.46 m and the highest common occurrence of *R. asanoi* (901 ka) at 18.37 m. Based on these tie points, we estimated an average sedimentation rate of ~8.6 cm.kyr^{-1} for the deposits correlating with Subchron C1r.1n (Jaramillo), a value that was lineary extrapolated to the 1.95 m lowermost part of the section. We further estimated an average sedimentation rate of ~10.2 cm.kyr^{-1} in the lower part of Subchron C1r.1r (Matuyama). In the absence of biostratigraphic and magnetostratigraphic tie points in the upper part of the section, we used the local oxygen isotopic stratigraphies. Between 24.77 m and 25.89 m, $\delta^{18}O$ values in *U. peregrina* and *G.*

bulloides decrease by about 1.78‰ and 1.73‰, respectively (Fig. 4, Table 1). Such sharp decreases are proposed to correlate with those occurring in LR04 benthic global $\delta^{18}O$ stack (Lisiecki and Raymo, 2005) and planktonic foraminiferal Mediterranean $\delta^{18}O$ Medstack (Wang et al., 2010) between Marine Isotope Stages (MIS) 22 and 21. In this re-examination of the age model of the northern Lindos Bay section, we assign the MIS 22/21 termination (866 ka; Lisiecki and Raymo, 2005) to 25.33 m. Such a level, characterized by a change in slope in both *U. peregrina* and *G. bulloides* $\delta^{18}O$ records, is proposed in agreement with those occurring in open-ocean reference records (Fig. 8; see section 5.2). Based on this tie point, we estimate an average sedimentation rate of ~19.8 cm.kyr^{-1} for the deposits occurring in the uppermost part of the section.

According to this age model, the samples analyzed in this study deposited between ~1100 ka and ~858 ka and the time interval between consecutive samples is estimated to range between 1 kyr (uppermost part of the section) and 4 kyr (lower part of the section) (Table 1). The sedimentation rates calculated for the northern Lindos Bay section appear on the whole much higher than in other exposures of the Lindos Bay Formation that benefited firm chronostratigraphic constraints. Average sedimentation rates of 2.93 cm.kyr^{-1} (Quillévéré et al., 2016), 3.15 cm.kyr^{-1} (Nouailhat, 2017), 3.6 cm.kyr^{-1} (Cornée et al., 2006b), and 4.35 cm.kyr^{-1} (Milker et al., 2017) were found in the Cape Vagia, Haraki, southern Lindos Bay and Pefka sections (Fig. 1C), respectively. The overall high sedimentation rates found in the continuous hemipelagic deposits of the northern Lindos Bay section further confirm that this section is ideal for high-resolution paleoclimatic and paleoenvironmental studies of the late Early Pleistocene of the eastern Mediterranean region.

5.2. A climate referential framework for the late Early Pleistocene of the eastern Mediterranean

Following our age model defined in the northern Lindos Bay section, we have reconstructed two independent and continuous $\delta^{18}O$ stratigraphies between ~1100 ka and ~858 ka, for the benthic foraminifera *Uvigerina peregrina* and for the planktonic foraminifera *Globigerina bulloides* (Figs. 8, 9). The lowest $\delta^{18}O$ values of *U. peregrina*, supposed to correlate with interglacial intervals, are in relatively good agreement with those of modern representatives of *Uvigerina* in the present-day eastern Mediterranean (average value of 2.14‰; Vergnaud Grazzini et al., 1986). Here, we interpret $\delta^{18}O$ values of *U. peregrina*, which are about >2.5‰, as reasonably reflecting glacial conditions. The $\delta^{18}O$ values of *G. bulloides* globally follow those of *U. peregrina*, with most shifts appearing nearly synchronous in both records. Again, the lowest $\delta^{18}O$ values of *G. bulloides* are in relatively good agreement with those of modern specimens of this species in the eastern Mediterranean (average value of 1.12‰; Vergnaud Grazzini et al., 1986).

In order to identify and characterize glacial-interglacial successions recorded in the studied section, the $\delta^{18}O$ stratigraphies were further independently correlated with open ocean $\delta^{18}O$ reference records (Fig. 8). The *U. peregrina* record is compared to the (1) astronomically-tuned LR04 benthic global stack of Lisiecki and Raymo (2005) and (2) benthic eastern Mediterranean records from ODP Sites 967 and 968 (Konijnendijk et al., 2015; Eratosthenes seamount, 2554 m and 1961 m respective water depths) compiled into a single splice by Konijnendijk et al. (2014). Overall, our bottom water record shows similar trends than those found in the open ocean and in the deep eastern Mediterranean Basin. Magnitudes of benthic $\delta^{18}O$ variations measured at Rhodes, are higher than those observed in the contemporaneous LR04. They are in agreement with those measured at ODP Sites 967/968 and exhibit an eastern Mediterranean deep-sea signature. Absolute $\delta^{18}O$ values measured in the northern Lindos Bay section are, on average, 2.60‰ more negative than those from the LR04, as expected in the semi-enclosed Mediterranean, which constitutes one of the

few warm deep-sea basins in the world. In the early part of the record (from ~1100 ka to ~930 ka), absolute $\delta^{18}O$ values in the northern Lindos Bay section appear remarkably similar to those of ODP Sites 967/968. This indicates that during this time interval, the studied section was exposed to water mass conditions comparable to those of the deep eastern Mediterranean Basin. Between ~930 ka and ~858 ka, however, absolute $\delta^{18}O$ values at Rhodes appear constantly offset by up to -1‰ compared to those of ODP Sites 967/968. Such lower $\delta^{18}O$ values at Rhodes may result from calcification of *U. peregrina* under higher bottom water temperatures (and/or less saline conditions). After ~930 ka, the northern Lindos Bay section may have been exposed to an increasing influence of shallower bottom waters. Such a hypothesis is first compabible with the apparent short-term ~200 m paleodepth decrease observed just before ~930 ka (Fig. 10C). It is also compatible with the $\delta^{13}C$ composition of *U. peregrina* (Fig. 10B), which shows significantly lower values after ~930 ka (on average -1.28‰) than between ~1100 ka and ~930 ka (on average -0.86%), possibly reflecting enhanced organic matter fluxes with decreasing paleodepths.

The *G. bulloides* record is compared with the planktonic Mediterranean database Medstack (Fig. 8) built by Wang et al. (2010) who compiled oxygen isotope compositions of the photosymbiotic, shallow-dwelling planktonic foraminifer *Globigerinoides ruber* measured in deep-sea core sequences of the central and eastern Mediterranean. We notice that the magnitudes of $\delta^{18}O$ variations measured on *G. bulloides* in the northern Lindos Bay section are smaller than those measured on *Gs. ruber* in the Medstack. While after ~930 ka $\delta^{18}O$ values from the Medstack and the northern Lindos Bay records are globally similar, they appear constantly offset of up ~1‰ between ~1100 ka and ~930 ka, confirming a deeper habitat in the surface waters (or cooler season of growth) for *G. bulloides* than for *Gs. ruber* (Schiebel and Hemleben, 2017).

Visual correlations between our benthic and planktonic $\delta^{18}O$ data-sets and their respective reference records (Fig. 8) indicate that the studied interval spans continuously from MIS 32 to MIS 21. We note, however, that the completeness of a glacial interval at the base of the section corresponding to MIS 32 has to be considered cautiously because it is supported by few isotopic data in a sedimentary interval where an extrapolated sedimentation rate (~8.6 $cm.kyr^{-1}$) was considered. In addition, within the LR04 stack, MIS 21 covers the interval between 866 ka and 814 ka. Regrettably, only the early part of this interglacial is recovered in the northern Lindos Bay section. Other correlations appear more powerful, both in terms of ages and durations. Our benthic and planktonic oxygen isotope records from the northern Lindos Bay section primarily follow changes in global ice volume, with trends in $\delta^{18}O$ changes appearing similar to those found in open ocean reference records.

Such a succession between MIS 32 and the early part of MIS 21, reconstructed from deposits exposed onshore, appears so far unique in the eastern Mediterranean. It provides a climate referential framework for the late Early Pleistocene, documenting a snapshot of the early stage of the EMPT in this region. At the scale of Quaternary climate changes, the EMPT marks a shift from 41 kyr-long symmetric climate cycles to 100 kyr-long asymmetric cycles. In detail, the duration and shape of climate cycles vary widely with possible pattern reversals, and regional effects in the mid-latitude Mediterranean Basin further render possible deviation from global climate trends (e.g., Colleoni et al., 2012). Compared to the $\delta^{18}O$ curves from benthic foraminifera stacked in LR04 (Lisiecki and Raymo, 2005) and compiled from ODP Sites 967/968 (Konijnendijk et al., 2015), benthic measurements in the northern Lindos Bay section show congruent interglacials: a long symmetric MIS 31, two long asymmetric MIS 25 and MIS 23 (Fig. 8). The most intriguing discrepancy between records comes from the multiple peaks observed within MIS 29 and MIS 27. While the LR04 curve makes clear a long glacial MIS 28 and a double-peak MIS 27, our record suggests two double peaks, each

associated with MIS 27 and MIS 29, respectively. Such features are shared with the ODP 967/968 benthic data compiled by Konijnendijk et al. (2015) and these pattern observations are confirmed by the planktonic $\delta^{18}O$ records (Fig. 8.) made available from the northern Lindos Bay section (this study) and the Medstack (Wang et al., 2010).

Spectral analyses performed independently on the *U. peregrina* and *G. bulloides* $\delta^{18}O$ data from the northern Lindos Bay section show average frequencies throughout the studied time interval (Fig. 9A). Both benthic and planktonic spectra only record one significant power peak at 41 kyr, indicating obliquity-paced $\delta^{18}O$ oscillations. Because spectrum analyses depend on the choosen time interval and its duration (especially during the onset of the EMPT characterized by changing frequency of cycles), only two spectra avalaible from the literature and based on benthic (Konijnendijk et al., 2015) and planktonic (Incarbona et al., 2013) Mediterranean data-sets can be used for comparison. They both suggest similar dominance at the 41 kyr frequency. Fortunatly, wavelet analyses allow vizualizing changes in power spectrum through time (Fig. 9B). They show that the planktonic $\delta^{18}O$ record exhibits a dominant precession frequency between ~1075 ka and ~980 ka (MIS 31 to MIS 27). When available, wavelet transform performed on various proxies extracted from sediments of the Mediterranean region show congruent and concomitant precession frequency. It includes pollens (Thenaghi Philippon section, Tzedakis et al., 2006; ODP Site 976, Joannin et al., 2011), clay mineral assemblages (ODP Site 964, Zhao et al., 2016), and planktonic foraminiferal stable isotopes (Montalbano Jonico, Girone et al., 2013). The common point between these proxies is that they all depend on atmospheric processes (plant growth, Saharian dust input, see surface temperatures). According to Zhao et al., (2016), reinforced precession cycles have had a significant influence on the African monsoon and have increased dust inputs into the central Mediterranean region. At Rhodes in the northern Lindos Bay section, we expect the $\delta^{18}O$ value drops to be caused by enhanced rainfall in phase with the

northward shift of the intertropical convergence zone (ITCZ) along with an increase in African monsoon strength during northern hemisphere orbital precession minima in the Mediterranean region (Kutzbach et al., 2014; Bosmans et al., 2015; Konijnendijk et al., 2015). Further studies focusing on the EMPT, both on land and at sea, improve our knowledge of atmospherical climate particularism in the Mediterranean from its western (Joannin et al., 2011; Oliveira et al., 2017) and central parts (Joannin et al., 2007b; 2008; Maiorano et al., 2008; Combourieu-Nebout et al., 2015; Capraro et al., 2017). This setting of regional climate particularisms is extended for the first time to the eastern part of the Mediterranean with the onshore record of the northern Lindos Bay section.

5.3. Planktonic foraminiferal assemblages within identified glacials and interglacials

During the late Early Pleistocene (late Calabrian) within the time interval considered in this study, the influence of global climate dynamics forcing on Mediterranean climate variability was increasing at the expense of regional processes (Colleoni et al., 2012). Consequently, if the stable isotope record chiefly reflects variations in global ice volume, the results of planktonic foraminiferal distribution in the northern Lindos Bay section may have resulted from sea-surface temperature changes over glacial-interglacial cycles. This relationship appears unclear since the 7 «warmer» and 7 «cooler» intervals inferred from clustering analysis performed on counts of planktonic foraminifera do not steadily and respectively match the glacials and interglacials recovered from the northern Lindos Bay section. The assemblages remain globally typical of the subtropical province (Bé, 1977) and reveal an unstable pattern of correlation with the isotope records on the long-term time scale (Fig. 10).

A clear relationship is particularly lacking when correlating with interglacials, probably because, in any case, oxygenated and stratified (sub)tropical surface waters mostly

permanently dominated the region, as indicated by the very high percentages of *Globigerinoides ruber* found throughout the section. For example, only MIS 31, MIS 29 and the recorded early part of MIS 21 are fully included in intervals in which the assemblages were permanently dominated by warmer species of planktonic foraminifera (Fig. 10). These intervals apparently started before and ended after the ranges of the related interglacials. The early part of MIS 27, and the late parts of MIS 25 and MIS 23, correlate with «warmer» surface temperatures in the studied area, but intervals with «cooler» species of planktonic foraminifera are superimposed to this pattern of warmer surface temperatures, possibly because of important short-term oscillations that portrayed these interglacials and the influence of a skipped deglaciation that has characterized MIS 23 (Tzedakis et al., 2017).

In the studied area, the global climate regime may have affected planktonic foraminiferal assemblages more clearly during glacials. Indeed, all glacials identified in the northern Lindos Bay section correlate with intervals in which surface waters are at least momentarily qualified as «cooler» based on the clustering analysis. MIS 26 fully correlates with an interval dominated by «cooler» assemblages of planktonic foraminifera. Remarkably, MIS 32, MIS 30, MIS 28, MIS 24 and MIS 22 all further show significant short-term influxes (>40%) of temperate to subpolar planktonic foraminifera (*Globorotalia inflata*, dextral *Neogloboquadrina pachyderma* and/or sinistral *Neogloboquadrina pachyderma*) and concomitant decreasing abundances of *G. ruber* (Fig. 10A). This may indicate that during the late Calabrian and off Rhodes, the ongoing increasing magnitude of high-latitude glacial-interglacial fluctuations that led to the EMPT had a significant impact on planktonic foraminiferal assemblages, allowing cool-water species to proliferate in surface waters, likely during glacial maxima.

It is noteworthy, however, that such significant influxes of cool-water species could also take place during interglacials, as shown in the MIS 27 record of the northern Lindos Bay

section (Fig. 10A, D). Apart from the influx at ~890 ka, a common point of the short-term (< ~10 kyr) influxes occurring both during glacial and interglacial periods is that they systematically match minima in the cycle of precession (Fig. 10E). Another common point of these short-term influxes is that they appear most often associated with depleted planktonic foraminiferal $\delta^{18}O$ values (Fig. 10B). Altogether, these characteristics bear a number of the hallmarks of the sapropel record that has been described in the eastern Mediterranean deep-sea. Indeed, studies of Pleistocene sapropels there have long shown that they correlate with (1) increasing abundances of temperate to subpolar planktonic foraminifera (e.g., Thunell et al., 1977; Cita et al., 1977), (2) precession minima (e.g., Rossignol-Strick et al., 1982; Rossignol-Strick, 1985), and (3) ^{18}O-depleted compositions of planktonic foraminifera (e.g., Rohling, 1994; Emeis et al., 2000). We consequently speculate that some of the oceanic events that led to the deposition of sapropels in the deep sea may have affected shallower environments along the eastern coast of Rhodes. Our planktonic foraminiferal assemblage data seem to support such a hypothesis. Considering our age model, there is indeed an apparent temporal correlation between short-term influxes of cool-water species (typified by *N. pachyderma* and *Gr. inflata*) in the northern Lindos Bay section (Fig. 10A) and the assigned ages of sapropels in the eastern Mediterranean deep sea (Fig. 10F; Kroon et al., 1998; Konijnendijk et al., 2014). We find, as a matter of fact, that nine of the eleven sapropels (i.e., all sapropels except S18 and S22) observed in the deep sea within the studied interval correlate with short-term influxes of cool-water species in the northern Lindos Bay section.

No lithologic indices of such oceanic events are visible in the field in the northern Lindos Bay section (e.g., layers enriched in organic matter, laminated layers), where the clays remain constantly massive and homogenous, but many laminated layers have been reported from other exposures of the Lindos Bay Formation (Fig. 1C) at Pefka (Milker et al., 2017) and Cape Vagia (Moissette and Spjeldnaes, 1995). At Kallithea, such laminated layers were even

interpreted as shallower water extensions of deep sea sapropels (Rasmussen and Thomsen, 2005) in levels which deposited nearly contemporaneously with the northern Lindos Bay section (Quillévéré et al., 2016). In the eastern Mediterranean, the formation of sapropels in the deep sea has generally been connected to the development of a higher stratification and/or productivity in the surface waters. The causes of such changes in the surface waters are still debated but enhanced precipitation and runoff of nutrient-rich waters from the Nile and Eurasian rivers are generally cited (e.g., Cramp and O'Sullivan, 1999; Rohling et al., 2015; Bosmans et al., 2015; Toucanne et al., 2015). Others associate river discharge to fresher Atlantic surface water contribution, slowing ventilation of the eastern Mediterranean Sea (Cornuault et al., 2016). This indicates that regional factors in the eastern Mediterranean influencing river discharges, have also played a crucial role on changes through time in the planktonic foraminiferal assemblages of the northern Lindos Bay section, explaining the complex and unstable pattern of correlation observed there between faunistic and stable isotope records.

5.4. Paleodepths and vertical motions in the northern Lindos Bay section

In Figure 10C, paleodepth estimates are corrected from the effect of relative sea-level changes by converting $\delta^{18}O$ Medstack values (Wang et al., 2010). A LOESS smoothing regression using PAST 3.22 (Hammer et al., 2001) further applied to these corrected paleodepths suggests that deposition occurred between ~150 m and ~450 m in the northern Lindos Bay section (Fig. 10C). The amount of uplift of this area located in the eastern coast of Rhodes is consistent with the marine terraces we observed at minimum elevations of 338 m above the Lindos Bay within the same basement block. Elsewhere, such a difference in elevation between the Lindos Bay Formation and the uppermost late Calabrian marine terraces reaches 448 m in the Pefka area and ~500 m in the Prophitis Elias Mountain near the

city of Cape Arkhangelos (Cornée et al., 2006a), thus in the order of the proposed maximum paleodepths. The estimated paleodepths and the observed general regressive trend (with shallowing depths found in the uppermost part of the section after ~870 ka), are also consistent with the results of Moissette and Spjeldnaes (1995) on the same section, which were based on the analysis of bryozoan assemblages at lower resolution, and suggested that deposition had occurred there between 200 m and 400 m. Our results consequently confirm that the northern Lindos Bay section deposited at upper bathyal depths during the late Calabrian.

The maximum paleodepths in the northern Lindos Bay section appear slightly lower than in many other studied exposures of the Lindos Bay Formation along the eastern coast of Rhodes, namely from south to north (Fig. 1C) at Pefka (610-650 m, Milker et al., 2017), Cape Vagia (300-500 m, Moissette and Spjeldnaes, 1995; 500-600 m, Van Hinsbergen et al., 2007; 300-475 m, Agiadi et al., 2018), and Vasfi (500-600 m, Moissette and Spjeldnaes, 1995). They are however in the same range as those estimated in the Lardos (320 m, Titschack et al., 2013; 200-400 m, Agiadi et al., 2018) and Kallithea (360-480 m, Rasmussen and Thomsen, 2005; 300-400 m, Agiadi et al., 2018) sections, which both expose more recent (i.e., late Calabrian to early Ionian) remnants of the Lindos Bay Formation, and deposited nearly contemporaneously with the northern Lindos Bay section (Quillévéré et al., 2016). These observations indicate that the phase of maximum transgression in the Lindos Bay Formation is not recovered in the northern Lindos Bay section, which deposited subsequently.

Our reconstruction also reveals repeated, though likely transient, paleodepth fluctuations with maximum amplitudes of up to ~200 m in the lower and middle parts of the section, between ~1070 ka and ~930 ka (Fig. 10C). Would these transient variations be entirely explained by tectonic adjustements, they would involve extremely rapid vertical motions, reaching minimum values of up to ~6 $mm.yr^{-1}$. Such rapid motions appear unlikely in the

context of the Hellenic forearc and in the Mediterranean region in general. Within and around the Hellenic forearc, the most important Pleistocene and Holocene uplift rates have been calculated in the Gulf of Corinth (2.4 to 3 $mm.yr^{-1}$; Stiros, 1998) or in southern Turkey (3.2 to 3.4 $mm.yr^{-1}$; Öğretmen et al., 2018) and values similar to those calculated from the northern Lindos Bay section appear only common in the context of very active forearcs, as for example at coastlines of the Andes Chain during the Holocene (Stefer et al., 2010). We consequently stress that the up to ~200 m amplitude transient depth changes found in the section may represent, at least partly, a sizable bias linked to local environmental changes (and resulting shifts in benthic foraminiferal taxa). Such kind of bias has already been observed at Rhodes in the Pefka section (Fig. 1C), in older deposits of the Lindos Bay Formation (Milker et al., 2017). Indeed, the ratio between planktonic and benthic foraminifera used in our reconstruction, even though primarily determined by depth, can be affected by changes in oxygenation of the bottom waters (e.g., Van der Zwaan et al., 1990). In particular, sedimentary intervals deposited at lower oxygenation concentrations have been shown to amplify the amplitude of P/P+B oscillations, including in settings of the Hellenic forearc (Van Hinsbergen et al., 2005). Although we note that the levels exhibiting the highest estimated paleodepths in the northern Lindos Bay section do not consistently match the occurrence of sapropels in the deep eastern Mediterranean (Fig. 10F), nor the high-amplitude precession minima (Fig. 10E), which have been found to result in higher export productivity and sapropel formation in the region (e.g., Rohling et al., 2015), changes in bottom water oxygenation may have indeed influenced the calculation of the amplitudes of vertical motions registered between ~1070 ka and ~930 ka. This would be not surprising because deep infaunal benthic foraminifera, whose increasing abundances indicate dysoxic conditions (Van der Zwaan et al., 1990), are indeed present in the record.

However, while their absolute amplitude values should be considered very cautiously, the occurrence of repeated and transient paleodepth variations in the upper bathyal depth domain, independent of climatic changes, may result from substantial local tectonic motions. At Pefka, 4.5 km south of the Lindos Bay (Fig. 1C), similar short-term paleodepth fluctuations, corrected from the potential effects of local environmental conditions and overprinted on the long-term transgressive-regressive trend, have already been characterized in early Calabrian deposits of the Lindos Bay Formation (Milker et al., 2017). Altogether, this suggests that deposition of the Lindos Bay Formation at Rhodes may have experienced a unique story of vertical motions during the Early Pleistocene, far more complex than the previously expected long-term scenario (e.g., Hanken et al., 1996; Cornée et al., 2006a).

The causes for such short-term repeated drowning and uplift events, recorded on the eastern coast of Rhodes at that time, may be best found in the context of the tremendous subsidence of the Rhodes Basin during the Plio-Pleistocene in combination with the oblique convergence occurring at the north-eastern end of the Hellenic forearc (e.g., Woodside et al., 2000; Ten Veen and Kleinspehn, 2002; Hall et al., 2009; Shaw and Jackson, 2010). Especially, the global eastward tilting of Rhodes responsible for the deposition of the bathyal clays of the Lindos Bay Formation (van Hinsbergen et al., 2007) may have acted not as a single and continuous event, but as a succession of short-term eastward tilting (drowning event) and westward backtilting (uplift event) episodes well-recorded in the ~1070-~930 ka interval. It is hypothesized that during the Early Pleistocene, such complex tectonic context involving successive compression and relaxation mechanisms has resulted in local, transient and potentially very rapid vertical motions along the eastern coast of Rhodes.

6. Conclusions

At Rhodes, the northern Lindos Bay section consists of 27 meters of very homogenous hemipelagic blue-grey clays lacking vertical facies changes and tectonic disturbances. It yields abundant, diversified and very well-preserved (micro)fossils. The foraminiferal assemblages indicate that the studied sediments deposited at upper bathyal depths between ~150 m and ~450 m. They additionnaly preserved a detailed and fairly time-constrained history of open-marine sedimentation for the late Early Pleistocene (late Calabrian) from the late part of geomagnetic Chron C1r.2r to the late part of Chron C1r.1 (Matuyama) between ~1100 ka and ~858 ka. In particular, the northern Lindos Bay section provides continuous stable isotope ($\delta^{18}O$, $\delta^{13}C$) and fossil records of glacial-interglacial successions from MIS 32 to the early part of MIS 21, allowing to connect the environmental changes that occurred regionally in the eastern Mediterranean with global climate cycles during the early stage of the EMPT. The section underwent severe uplift since the late Early Pleistocene and is today easily accessible onshore. These characteristics, gathered together, demonstrate that the northern Lindos Bay section constitutes an important, useful and most probably unique archive for understanding the climatic, environmental and tectonic evolution of the eastern Mediterranean region during an important interval of Earth's history.

Acknowledgments

We warmly thank Jean Goedert and Abel Barral for technical assistance with the mass spectrometer and and Frans Jorissen for helpful discussions. We would also like to thank Yvonne Milker, an anonymous reviewer and the Editor Henning Bauch who provided constructive comments that helped us to improve the present paper. This work was supported by the National Research programs Tellus-INTERRVIE (FQ) and Tellus-SYSTER (JJC) of CNRS-INSU.

Appendix A

Supplementary Table S1. Counts of foraminifera in samples collected from the northern Lindos Bay Section. Counts of pollen, not discussed in this paper, are also provided in this supplementary file.

References

1. Agiadi, K., Girone, A., Koskeridou, E., Moissette, P., Cornée, J.-J., Quillévéré, F., 2018. Pleistocene marine fish invasions and paleoenvironmental reconstructions in the eastern Mediterranean. Quaternary Science Reviews 196, 80–99.
2. André, A., Weiner, A., Quillévéré, F., Aurahs, R., Morard, R., Douady, C.J., de Garidel-Thoron, T., Escarguel, G., de Vargas, C., Kucera, M., 2013. The cryptic and the apparent reversed: lack of genetic differentiation within the morphologically diverse plexus of the planktonic foraminifer *Globigerinoides sacculifer*. Paleobiology 39(1), 21–39.
3. Backman, J., Raffi, I., Rio, D., Fornaciari, E., Pälike, H., 2012. Biozonation and biochronology of Miocene through Pleistocene calcareous nannofossils from low and middle latitudes. Newsletters on Stratigraphy 45, 221–224.
4. Bé, A.W.H., 1977. An ecological, zoogeographical and taxonomic review of Recent planktonic foraminifera. In: Ramsay, A.T.S. (Ed.), Oceanic Micropaleontology, vol. 1. Academic Press, London, pp. 1–100.
5. Berger, W.H., Diester-Haas, L., 1988. Paleoproductivity: the benthic/planktonic ratio in foraminifera as a productivity index. Marine Geology 81, 15–25.
6. Bosmans, J.H.C., Drijfhout, S.S., Tuenter, E., Hilgen, F.J., Lourens, L.J., Rohling, E.J., 2015. Precession and obliquity forcing of the freshwater budget over the Mediterranean. Quaternary Science Reviews 123, 16–30.

7. Capraro, L., Ferretti, P., Macri, P., Scarponi, D., Tateo, F., Fornaciari, E., Bellini, G., Dalan, G., 2017. The Valle di Manche section (Calabria, Southern Italy): a high resolution record of the Early-Middle Pleistocene transition (MIS-21-MIS19) in the Central Mediterranean. Quaternary Science Reviews 165, 31–48.
8. Ciaranfi, N., Lirer, F., Lirer, L., Lourens, L.J., Maiorano, P., Marino, M., Petrosino, P., Sprovieri, M., Stefanelli, S., Brilli, M., Girone, A., Joannin, S., Pelosi, N., Vallefuoco, M., 2010. Integrated stratigraphy and astronomical tuning of lower-middle Pleistocene Montalbano Jonico section (southern Italy). Quaternary International 219, 109–120.
9. Cita, M.B., Vergnaud-Grazzini, C., Robert, C., Chamley, H., Giaranfi, N, D'Onofrio, S., 1977. Paleoclimatic record of a long deep sea core from the eastern Mediterranean: Quaternary Research 8, 205–235.
10. Clark, P.U., Archer, D., Pollard, D., Blum, J.D., Rial, J.A., Brovkin, V., Mix, A.C., Pisias, N.G., Roy, M., 2006. The middle Pleistocene transition: characteristics, mechanisms, and implications for long-term changes in atmospheric pCO_2. Quaternary Science Reviews 25 (23-24), 3150–3184.
11. Colleoni, F., Masina, S., Negri, A., Marzocchi, A., 2012. Plio-Pleistocene high-low latitude climate interplay: a Mediterranean point of view. Earth and Planetary Science Letters 319-320, 35–44.
12. Combourieu-Nebout, N., Bertini, A., Russo-Ermolli, E., Peyron, O., Klotz, S., Montade, V., Fauquette, S., Allen, J., Fusco, F., Goring, S., Huntley, B., Joannin, S., Lebreton, V., Magri, D., Martinetto, E., Orain, R., Sadori, L., 2015. Climate changes in Central Mediterranean and Italian vegetation dynamics since the Pliocene. Review of Paleobotany and Palynology 218, 127–147.

13. Cornée, J.-J., Quillévéré, F., Moissette, P., Fietzke, J., Lopez-Otalvaro, G.E., Melinte-Dobrinescu, M.C., Philippon, M., van Hinsbergen, D.J.J., Agiadi, K., Koskeridou, E., Münch, P. 2019. Tectonic motion in oblique subduction forearcs: insights from the revisited Middle and Upper Pleistocene deposits of Rhodes, Greece. Journal of the Geological Society 176, 78–96.
14. Cornée, J.-J., Moissette, P., Joannin, S., Suc, J.-P., Quillévéré, F., Krijgsman, W., Hilgen, F., Koskeridou, E., Münch, P., Lécuyer, C., Desvignes, P., 2006a. Tectonic and climatic controls on coastal sedimentation: the Late Pliocene-Middle Pleistocene of northeastern Rhodes, Greece. Sedimentary Geology 187, 159–181.
15. Cornée, J.-J., Münch, P., Quillévéré, F., Moissette, P., Vasiliev, I., Krijgsman, W., Verati, C., Lécuyer, C., 2006b. Timing of Late Pliocene to Middle Pleistocene tectonic events in Rhodes (Greece) inferred from magneto-stratigraphy and $^{40}Ar/^{39}Ar$ dating of a volcanoclastic layer. Earth and Planetary Science Letters 250, 281–291.
16. Cornuault, M., Vidal, L., Tachikawa, K., Licari, L., Rouaud, G., Sonzogni, C., Revel, M. 2016. Deep water circulation within the eastern Mediterranean Sea over the last 95 kyr: New insights from stable isotopes and benthic foraminiferal assemblages. Palaeogeography, Palaeoclimatology, Palaeoecology, 459: 1–14.
17. Cramp, A., O'Sullivan, G., 1999. Neogene sapropels in the Mediterranean: a review. Marine Geology 153, 11–28.
18. Duermeijer, C.E., Nyst, M., Meijer, P.T., Langereis, C.G., Spakman, W., 2000. Neogene evolution of the Aegean Arc; paleomagnetic and geodetic evidence for a rapid and young rotation phase. Earth and Planetary Science Letters 176, 509–525.
19. Elderfield, H., Ferretti, P., Greaves, M., Crowhurst, S.J., McCave, I.N., Hodell, D., Piotrowski, A., 2012. Evolution of ocean temperature and ice volume through the mid Pleistocene climate transition. Science 337, 704–709.

20. Emeis, K.-C., Sakamoto, T., Wehausen, R., Brumsack, H.-J., 2000. The sapropel record of the eastern Mediterranean Sea – results of Ocean Drilling Program Leg 160. Palaeogeography, Palaeoclimatology, Palaeoecology 158, 371–395.
21. Emig, C.C., 1997. Bathyal zones of the Mediterranean continental slope: an attempt. Publicaciones Especiales del Instituto Espanol de Oceanografia 23, 23–33.
22. Fourel, F., Martineau, F., Tóth, E., Görög, A., Escarguel, G., Lécuyer, C., 2015. Carbon and oxygen isotope variability among foraminifera and ostracod carbonated shells. Annales Universitaties Mariae Curie-Sklodowska Sectio AAA Physica 70, 133–156.
23. Gibson, T.G., 1989. Planktonic-benthonic foraminiferal ratios: modern patterns and Tertiary applicability. Marine Micropaleontology 15, 29–52.
24. Girone, A., Capotondi, L., Ciaranfi, N., Di Leo, P., Lirer, F., Maiorano, P., Marino, M., Pelosi, N., Pulice, I., 2013. Paleoenvironmental changes at the lower Pleistocene Montalbano Jonico section (southern Italy): Global versus regional signals. Palaeogeography, Palaeoclimatology, Palaeoecology 371, 62–79.
25. Hall, J., Aksu, A.E., Elitez, I., Yaltirak, C., Cifçi, G., 2014. The Fethiye-Burdur Fault Zone: a component of upper plate extension of the subduction transform edge propagator fault linking Hellenic and Cyprus Arcs, Eastern Mediterranean. Tectonophysics 635, 89–99.
26. Hall, J., Aksu, A.E., Yaltirak, C., Winsor, J.D., 2009. Structural architecture of the Rhodes Basin: a deep depocentre that evolved since the Pliocene at the junction of Hellenic and Cyprus Arcs, eastern Mediterranean. Marine Geology 258 (1–4), 1–23.
27. Hammer, O., Harper, D.A.T., Ryan, P.D., 2001. PAST: paleontological statistics software package for education and data analysis. Palaeontologica Electronica 4(1), 1–9.

28. Hanken, N.-M., Bromley, R.G., Miller, J., 1996. Plio-Pleistocene sedimentation in coastal grabens, north-east Rhodes, Greece. Geological Journal 21, 271–296.
29. Hansen, K.S., 1999. Development of a prograding carbonate wedge during sea level fall: lower Pleistocene of Rhodes, Greece. Sedimentology 46, 559–576.
30. Head, M.J., Gibbard, P.L., 2015. Early-Middle Pleistocene transitions: linking terrestrial and marine realms. Quaternary International 389, 7–46.
31. Joannin, S., Bassinot, F., Combourieu Nebout, N., Peyron, O., Beaudouin, C., 2011. Vegetation response to obliquity and precession forcing during the Mid Pleistocene Transition in Western Mediterranean region (ODP Site 976). Quaternary Science Reviews 30, 280–297.
32. Joannin, S., Ciaranfi, N., Stefanelli, S., 2008. Vegetation changes during the late Early Pleistocene at Montalbano Jonico (Province of Matera, southern Italy) based on pollen analysis. Palaeogeography, Palaeoclimatology, Palaeoecology 270, 92–101.
33. Joannin, S., Cornée, J.-J., Moissette, P., Suc, J.-P., Koskeridou, E., Lécuyer, C., Buisine, C., Kouli, E., Ferry, S., 2007a. Changes in vegetation and marine environments in the eastern Mediterranean (Rhodes Island, Greece) during the Early and Middle Pleistocene. Journal of the Geological Society 164, 1119–1131.
34. Joannin, S., Quillévéré, F., Suc, J.-P., Lécuyer, C., Martineau, F., 2007b. Early Pleistocene climate changes in the central Mediterranean region as inferred from integrated pollen and planktonic foraminiferal stable isotope analyses. Quaternary Research 67, 264–274.
35. Kennett, J.P., Srinivasan, M.S. (Eds), 1983. Neogene planktonic foraminifera, A Phylogenetic Atlas. Hutchinson Ross Publishing Company, Stroudsburd, Pennsylvania, 265 pp.

36. Konijnendijk, T.Y.M., Ziegler, M., Lourens L.J., 2015. On the timing and forcing mechanisms of late Pleistocene glacial terminations: Insights from a new high-resolution benthic stable oxygen isotope record of the eastern Mediterranean. Quaternary Science Reviews 129, 308–320.
37. Konijnendijk, T.Y.M., Ziegler, M., Lourens, L.J., 2014. Chronological constraints on Pleistocene sapropel depositions from high-resolution geochemical records of ODP Sites 967 and 968. Newsletters on Stratigraphy 47(3), 263–282.
38. Kovacs, E., Spjeldnaes, N., 1999. Pliocene-Pleistocene stratigraphy of Rhodes, Greece. Newsletters on Stratigraphy 37, 191–208.
39. Kroon, D., Alexander, I., Little, M., Lourens, L.J., Matthewson, A., Robertson, A.H.F., Sakamoto, T., 1998. Oxygen isotope and sapropel stratigraphy in the eastern Mediterranean during the last 3.2 million years. In: Robertson, A.H.F., Emeis, K.-C., Richter, C., Camerlenghi, A. (Eds), Proceedings of the Ocean Drilling Program, Scientific Results, vol. 160, pp. 181–189.
40. Kutzbach, J.E., Chen, G., Cheng, H., Edwards, R.L., Liu, Z., 2014. Potential role of winter rainfall in explaining increased moisture in the Mediterranean and Middle East during periods of maximum orbitally-forced insolation seasonality. Climate Dynamics 42(3–4), 1079–1095.
41. Laskar, J., Robutel, P., Joutel, F., Gastineau, M., Correia, A.C.M., Levrard, B., 2004. A long-term numerical solution for the insolation quantities of the Earth. Astronomy and Astrophysics 428, 261–285.
42. Lécuyer, C., Daux, V., Moissette, P., Cornée, J.-J., Quillévéré, F., Koskeridou, E., Fourel, F., Martineau, F., Reynard, B., 2012. Stable carbon and oxygen isotope compositions of invertebrate coarbonate shells and the reconstruction of

paleotemperatures and paleosalinities: a case study of the early Pleistocene of Rhodes, Greece. Palaeogeography, Palaeoclimatology, Palaeoecology 350-352, 39–48.

43. Lisieki, L.E., Raymo, M.E., 2007. Plio-Pleistocene climate evolution: trends and transitions in glacial cycle dynamics. Quaternary Science Reviews 26, 56–69.
44. Lisiecki, L.E., Raymo, M.E., 2005. A Pliocene-Pleistocene stack of 57 globally distributed benthic $\delta^{18}O$ records. Paleoceanography 20, 1–17.
45. Lourens, L.J., Hilgen, F.J., Laskar, J., Shackleton, N.J., Wilson, D., 2005. The Neogene period. In: Gradstein, F.M., Ogg, J.G., Smith, A.G. (Eds), A Geological Time Scale 2004. Cambridge University Press, pp. 409–440.
46. Løvlie, R., Støle, G., Spjeldnaes, N., 1989. Magnetic polarity stratigraphy of Pliocene-Pleistocene marine sediments from Rhodos, eastern Mediterranean. Physics of the Earth and Planetary Interiors 54, 340–352.
47. Maiorano, P., Aiello, G., Barra, D., Di Leo, P., Joannin, S., Lirer, F., Marino, M., Pappalardo, A., Capotondi, L., Ciaranfi, N., Stefanelli, S., 2008. Paleoenvironmental changes during sapropel 19 (i-cycle 90) deposition: evidences from geochemical, mineralogical and micropaleontological proxies in the mid-Pleistocene Montalbano Jonico land section (Southern Italy). Palaeogeography, Palaeoclimatology, Palaeoecology 257, 308–334.
48. Meulenkamp, J.E., de Mulder, E.F.J., Van der Weerd, A., 1972. Sedimentary history and paleogeography of the Late Cenozoic of the island of Rhodos. Zeitschrift der Deutschen Geologischen Gesellschaft 123, 541–553.
49. Milker, Y., Weinkauf, M.F.G., Titschack, J., Freiwald, A., Krüger, A., Jorissen, F.J., Schmiedl, G., 2017. Testing the applicability of a benthic foraminiferal-based transfer function for the reconstruction of paleowater depth changes in Rhodes (Greece) during the early Pleistocene. PLoS ONE 12(11):e0188447.

50. Moissette, P., Koskeridou, E., Drinia, H., Cornée, J.-J., 2016. Facies associations in warm-temperate siliciclastic deposits: insights from early Pleistocene eastern Mediterranean (Rhodes, Greece). Geological Magazine 153, 61–83.
51. Moissette, P., Koskeridou, E., Conrée, J.J., André, J.P., 2013. Fossil assemblages associated with submerged beachrock beds as indicators of environmental changes in terrigenous sediments: examples from the Gelasian (Early Pleistocene) of Rhodes, Greece. Palaeogeography, Palaeoclimatology, Palaeoecology 369, 14–27.
52. Moissette, P., Koskeridou, E., Cornée, J.-J., Guillocheau, F., Lécuyer, C., 2007. Spectacular preservation of seagrasses and seagrass-associated communities from the Pliocene of Rhodes, Greece. Palaios 22, 200–211.
53. Moissette, P., Spjeldnaes, N., 1995. Plio-Pleistocene deep-water bryozoans from Rhodes, Greece. Palaeontology 38, 771–799.
54. Murray, J.W., 1991. Ecology and Palaeoecoloy of Benthic Foraminifera. Longman Harlow, Harlow, 397 pp.
55. Mutti, E., Orombelli, G., Pozzi, R., 1970. Geological studies on the Dodecanese islands (Aegean Sea). IX. Geological map of the island of Rhodes (Greece); explanatory notes. Annales Géologiques des Pays Helléniques 22, 79–226.
56. Nouailhat, N., 2017. Elaboration d'un référentiel paléoclimatique pour le Pléistocène inférieur de Méditerranée orientale. Université Rennes 1, Ms-Thesis Préhistoire-Paléontologie-Paléoenvironnement (unpublished), 31 pp.
57. Öğretmen, N., Cipollari, P., Frezza, V., Faranda, C., Karanika, K., Gliozzi, E., Radeff, G., Cosentino, D., 2018. Evidence for 1.5 km of uplift of the Central Anatolian Plateau's southern margin in the last 450 kyr and implications for its multi-phased uplift history. Tectonics 37, 359–390.

58. Oliveira, D., Sánchez Goñi, M.F., Naughton, F., Polanco-Martínez, J.M., Jimenez-Espejo, F.J., Grimalt, J.O., Martrat, B., Voelker, A.H.L., Trigo, R., Hodell, D., Abrantes, F., Desprat, S., 2017. Unexpected weak seasonal climate in the western Mediterranean region during MIS 31, a high-insolation forced interglacial. Quaternary Science Reviews 161, 1–17.
59. Papanikolaou, M.D., Triantaphyllou, M.V., Platzman, E.S., Gibbard, P.L., Mac Niocaill, C., Head, M.J., 2011. A well-established early-middle Pleistocene marine sequence on south-east Zakynthos island, western Greece: magneto-biostratigraphic constraints and paleoclimatic implications. Journal of Quaternary Science 26(5), 523–540.
60. Pujol, C., Vergnaud Grazzini, C., 1995. Distribution of live planktonic foraminifers as related to regional hydrography and productive systems of the Mediterranean Sea. Marine Micropaleontology 25, 187–217.
61. Quillévéré, F., Cornée, J.-J., Moissette, P., López-Otálvaro, G.E., van Baak, C., Münch, P., Melinte-Dobrinescu, M.C., Krijgsman, W., 2016. Chronostratigraphy of uplifted Quaternary hemipelagic deposits from the Dodecanese island of Rhodes (Greece). Quaternary Research 86, 79–94.
62. Rasmussen, T.L., Thomsen, E., 2005. Foraminifera and paleoenvironments of the Plio-Pleistocene Kallithea Bay Section, Rhodes, Greece: evidence for cyclic sedimentation and shallow-water sapropels. Cushman Foundation Special Publication 39, 15–51.
63. Rio, D., Channel, J.E.T., Massari, F., Poli, M.S., Sgavetti, M., D'Allessandro, A., Prosser, G., 1996. Reading Pleistocene eustasy in a tectonically active siliciclastic shelf setting (Crotone peninsula, southern Italy). Geology 24, 743–746.

64. Rohling, E.J., 1994. Review and new aspects concerning the formation of eastern Mediterranean sapropels. Marine Geology 122, 1–28.

65. Rohling, E.J., Marino, G., Grant, K.M., 2015. Mediterranean climate and oceanography, and the periodic development of anoxix events (sapropels). Earth-Science Reviews 143, 62–97.

66. Rohling, E.J., Foster, G.L., Grant, K.M., Marino, G., Roberts, A.P., Tamisiea, M.E., Williams, F., 2014. Sea-level and deep-sea temperature variability over the past 5.3 million years. Nature 508, 477–482.

67. Rossignol-Strick, M., 1985. Mediterranean Quaternary sapropels, an immediate response of the African monsoon to variation of insolation. Palaeogeography, Palaeoclimatology, Palaeoecology 49, 237–263.

68. Rossignol-Strick, M., Nesteroff, V., Olive, P., Vergnaud-Grazzini, C., 1982. After the deluge: Mediterranean stagnation and sapropel formation. Nature 295, 105–110.

69. Ruddiman, W.F., Raymo, M.E., Martinson, D.G., Clement, B.M., Backman, J., 1989. Pleistocene evolution: northern hemisphere ice sheets and North Atlantic Ocean. Paleoceanography 4, 353–412.

70. Schiebel, R., Hemleben, C., 2017. Planktonic foraminifers in the modern Ocean. Springer-Verlag Berlin Heidelberg, 358 pp.

71. Schulz, M., Mudelsee, M., 2002. REDFIT: estimating red-noise spectra directly from unevenly spaced paleoclimatic time seraies. Computers & Geosciences 28, 421–426.

72. Shaw, B., Jackson, J., 2010. Earthquake mechanisms and active tectonics of the Hellenic subduction zone. Geophysical Journal International 181, 966–984.

73. Stefer, S., Moernaut, J., Melnick, D., Echter, H.P., Arz, H.W., Lamy, F., De Batists, M., Oncken, O., Haug, G.H., 2010. Forearc uplift rates deduced from sediment cores of two coastal lakes in south-central Chile. Tectonophysics 495(1), 129–143.

74. Steinthorsdottir, M., Hakansson, E., 2017. Endo- and epilithic faunal succession in a Pliocene-Pleistocene cave on Rhodes, Greece: record of a transgression. Palaeontology 60, 663–681.

75. Steinthorsdottir, M., Lidgard, S., Hakansson, E., 2006. Fossils, sediments, tectonics. Reconstructing palaeoenvironments in a Pliocene-Pleistocene Mediterranean microbasin. Facies 52, 361–380.

76. Stiros, S.C., 1998. Archaeological evidence for unusually rapid Holocene uplift rates in an active normal faulting terrain: Roman harbour of Aigeira, Gulf of Corinth, Greece. Geoarchaeology 13, 731–741.

77. Ten Veen, J.H., Kleinspehn, K.L., 2002. Geodynamics along an increasingly curved convergent plate margin: Late Miocene-Pleistocene Rhodes, Greece. Tectonics 21, 1–21.

78. Thomsen, E., Rasmussen, T.L., Hastrup, A., 2001. Calcareous nannofossil, ostracode and foraminifera biostratigraphy of Plio-Pleistocene deposits, Rhodes (Greece), with correlation to the Vrica section (Italy). Journal of Micropalaeontology 20, 143–154.

79. Thunell, R.C., Williams, D.F., Kennett, 1977. Late Quaternary paleoclimatology, stratigraphy and sapropel history in eastern Mediterranean deep-sea sediments. Marine Micropaleontology 2, 371–388.

80. Titschack, J., Joseph, N., Fietzke, J., Freiwald, A., Bromley, R.G., 2013. Record of a tectonically-controlled regression captured by changes in carbonate skeletal associations on a structured island shelf (mid-Pleistocene, Rhodes, Greece). Sedimentary Geology 283, 15–33.

81. Titschack, J., Nelson, C.S., Beck, T., Freiwald, A., Radtke, U., 2008. Sedimentary evolution of a late Pleistocene temperate red algal reef (Coralligène) on Rhodes, Greece: correlation with global sea-level fluctuations. Sedimentology 55, 1747–1776.

82. Titschack, J., Bromley, R.G., Freiwald, A., 2005. Plio-Pleistocene cliff-bound, wedge-shaped, warm-remperate carbonate deposits from Rhodes (Greece): sedimentology and facies. Sedimentary Geology 180, 29–56.

83. Titschack, J., Freiwald, A., 2005. Growth, deposition, and facies of Pleistocene bathyal coral communities from Rhodes, Greece. In Cold-water Corals and Ecosystems, A. Freiwald & J.M. Roberts (Eds.), Berlin, Heidelberg: Springer-Verlag, pp. 41–59.

84. Toucanne, S., Minto'o, M.A., Fontanier, C., Bassetti, M.A., Jorry, S.J., Jouet, G., 2015. Tracking rainfall in the northern Mediterranean borderlands during sapropel deposition. Quaternary Science Reviews 129, 178–195.

85. Tzedakis, P.C., Crucifix, M., Mitsui, T., Wolff, E.W., 2017. A simple rule to determine which insolation cycles lead to interglacials. Nature 542, 427–432.

86. Tzedakis, P.C., Hooghiemstra, H., Pälike, H., 2006. The last 1.35 million years at Tenaghi Philippon: revised chronostratigraphy and long-term vegetation trends. Quanternary Science Reviews 25, 3416–3430.

87. Van der Zwaan, G.J., Jorissen, F.J., De Stigter, H.C., 1990. The depth dependency of planktonic/benthic foraminiferal ratios: Constraints and applications. Marine Geology 95, 1–16.

88. Van Hinsbergen, D.J.J., Krijgsman, W., Langereis, W., Cornée, J.-J., Duermeijer, C.E., Van Vugt, N., 2007. Discrete Plio-Pleistocene phases of tilting and counterclockwise rotation in the southeastern Aegean arc (Rhodes, Greece): early Pliocene formation of the south Aegean left-lateral strike-slip system. Journal of the Geological Society of London 164, 1133–1144.

89. Van Hinsbergen, D.J.J., Kouwenhoven, T.J., van der Zwaan, G.J., 2005. Paleobathymetry in the backstripping procedure: correction for oxygenation effects on depths estimates. Palaeogeography, Palaeoclimatology, Palaeoecology 221, 245–265.
90. Vergnaud Grazzini, C., Devaux, M., Znaidi, J., 1986. Stable isotope "anomalies" in Mediterranean Pleistocene records. Marine Micropaleontology 10, 35–69.
91. Wang, P., Tian, J., Lourens, L.J., 2010. Obscuring of long eccentricity cyclicity in Pleistocene oceanic carbon isotope records. Earth and Planetary Science Letters 290, 319–330.
92. Woodside, J., Mascle, J., Volkonskaia, A., 2000. The Rhodes Basin, a post-Miocene tectonic trough. Marine Geology 165, 1–12.
93. Zavatavielli, M., Mellor, G.L., 1995. A numerical study of the Mediterranean Sea circulation. Journal of Physical Oceanography 25, 1384–1414.
94. Zhao, Y., Colin, C., Liu, Z., Bonneau, L., Siani, G., 2016. Climate forcing of terrigenous sediment input to the central Mediterranean Sea since the early Pleistocene. Palaeogeography, Palaeoclimatology, Palaeoecology 442, 23–35.

Figure captions

Fig. 1. Location maps of the island of Rhodes (A) in the Mediterranean, and (B) simplified geodymamic context in the eastern Mediterranean (modified from Meulenkamp et al., 1972; Hall et al., 2014; Cornée et al., 2019). (C) Simplified geological map of Rhodes (modified from Mutti et al., 1970) with location of the Lindos Bay and other localities mentioned in this paper. (D) Field view and lithostratigraphy of the studied northern Lindos Bay section, photographed from the southern side of the Lindos Bay. (E) Log of the studied section

showing location of the collected samples, with calcareous nannofossil biostratigraphic and magnetostratigraphic data from Quillévéré et al. (2016).

Fig. 2. Lithostratigraphic scheme for the Pleistocene deposits of the eastern coast of Rhodes (modified from Cornée et al., 2019) with formations in the left panel and synthems (with associated published ages) in the right panel. The different formations of the Rhodes synthem (including the studied Lindos Bay Formation) are shown in color (SPB: Saint Paul's Bay Formatin). The lithology of the formations of the other synthems are detailed in Cornée et al. (2019).

Fig. 3. (A) Scanning electron (SEM) microphotographs of representative benthic (1) and planktonic (2) foraminifera picked for stable isotope analyses. (1) *Uvigerina peregrina* in umbilical (a) and microstructure (b) views; (2) *Globigerina bulloides* in umbilical (a) and microstructure (b) views. Scale bars = 100 µm (a) and 10 µm (b). (B) SEM microphotographs of representative specimens of other planktonic foraminiferal taxa identified in the northern Lindos Bay section. (1) *Orbulina universa*; (2) *Globigerinoides ruber* in umbilical view; (3) *Globigerinoides conglobatus* in umbilical (a) and spiral (b) views; (4) *Trilobatus sacculifer* in umbilical view; (5) *Globigerinella siphonifera* in edge (a) and umbilical (b) views; (6) *Globigerinita glutinata* in umbilical view; (7) *Beella digitata* in umbilical view; (8) *Turborotalia quinqueloba* in umbilical view; (9) *Sphaeroidinella dehiscens* in umbilical (a) and spiral (b) views; (10) dextral morphotype of *Neogloboquadrina pachyderma* in umbilical view; (11) sinistral morphotype of *Neogloboquadrina pachyderma* in umbilical view; (12) *Globorotalia inflata* in umbilical view; (13) sinistral morphotype of *Globorotalia crassaformis* in umbilical (a) and edge (b) views; (14) dextral morphotype of *Globorotalia*

truncatulinoides in umbilical (a) and edge (b) views; (15) *Globorotalia scitula* in umbilical view. Scale bars = 100 µm.

Fig. 4. Benthic (*Uvigerina peregrina*) and planktonic (*Globigerina bulloides*) foraminiferal stable isotope ($\delta^{18}O_{VPDB}$ and $\delta^{13}C_{VPDB}$) stratigraphic records of the northern Lindos Bay section.

Fig. 5. Results of foraminiferal counts in the northern Lindos Bay section. (A) Frequency curves (%) of the planktonic foraminiferal taxa and morphotypes. (B) Stratigraphically constrained dendrogram resulting from the UPGMA hierarchical clustering of the Bray-Curtis similarity matrix related to the sampled raw foraminiferal abundances (the dashed horizontal lines separate the significantly different clusters identified through overall and pairwise ANOSIMs). (C) First axis score (blue curve) resulting from the Correspondence Analysis (CA) of the raw abundances of the 20 taxa and morphotypes of planktonic foraminifera sampled in the studied section. This first CA-axis score is used to assign a probable ecological habitat to the clusters of planktonic foraminiferal assemblages identified by the hCA and ANOSIMs procedure, distinguishing between «warmer» (CA-1 > 0) and «cooler» (CA-1 < 0) assemblages. (D) P/P+B ratios (calculated for each sample based on the number of planktonic foraminifera relative to the total number of foraminifera), with the black vertical line deliminating samples that deposited in the upper bathyal zone (P/P+B > 0.70) and in the outer shelf zone (P/P+B < 0.70) following Murray (1991). (E) Associated paleodepths (grey line) estimated after Gibson (1989) with values corrected from the effect of glacio-eustatic sea-level changes (red line).

Fig. 6. Histogram showing the contribution of the 20 planktonic foraminiferal taxa and morphotypes to the first axis of the Correspondence Analysis (CA) of the 98 fossil assemblages studied from the northern Lindos Bay section. *B.* = *Beella*; *G.* = *Globigerina*; *Ga.* = *Globigerinita*; *Ge.* = *Globigerinella*; *Gr.* = *Globorotalia; Gs.* = *Globigerinoides; Sa.* = *Sphaeroidinella*; *T.* = *Trilobatus*; *Tr.* = *Turborotalita*.

Fig. 7. Age model and linear sedimentation rates estimated between tie points for the late Early Pleistocene (late Calabrian) deposits of the northern Lindos Bay section. The age model is mainly based on biostratigraphic and magnetostratigraphic data by Quillévéré et al. (2016). Error bars represent sample spacing for biostratigraphy (blue) and magnetostratigraphy (grey) in Quillévéré et al. (2016). Lacking biostratigraphic and magnetostratigraphic tie points to estimate a sedimentation rate in the uppermost part of the section, we u the reconstructed $\delta^{18}O$ stratigraphies to localize the MIS 22/21 termination (866 ka; Lisiecki and Raymo, 2005) at the altitude of 25.33 m. GPTS and CNPL (Calcareous Nannofossil Plio-Pleistocene) zonal scheme by Lourens et al. (2005) and Backman et al. (2012), respectively.

Fig. 8. Proposed correlation between the benthic (*Uvigerina peregrina*, black bold line) and planktonic (*Globigerina bulloides*, blue bold line) foraminiferal oxygen isotope ($\delta^{18}O_{VPDB}$) records of the northern Lindos Bay section and open ocean $\delta^{18}O$ reference records. Open ocean reference records include the LR04 benthic global $\delta^{18}O$ stack (Lisiecki and Raymo, 2005), the benthic eastern Mediterranean $\delta^{18}O$ compilation data from ODP Sites 967 and 968 (Konijnendijk et al., 2015), and the planktonic foraminiferal eastern Mediterranean $\delta^{18}O$ Medstack (Wang et al., 2010). The coincidence of successive positive and negative excursions in all $\delta^{18}O$ records reveals the identification, in the northern Lindos Bay section, of 12 distinct

isotopic stages between MIS 32 and the early part of MIS 21, including 6 interglacials (grey areas) and 6 glacials (white areas). GPTS by Lourens et al. (2005).

Fig. 9. Results of the power spectrum (A) and wavelet transform (B) analyses of the planktonic (*G. bulloides*, blue line, upper panel) and benthic (*U. peregrina*, black line, lower panel) foraminiferal oxygen isotope ($\delta^{18}O_{VPDB}$) records of the northern Lindos Bay section. Spectra show a dominant peak at 41 kyr. The cones of influence plotted on scalograms (B) show the region where boundary effects are present. Horizontal bars in B indicate the standard Milankovic 100-kyr, 41-kyr, and 23-19-kyr periodicities.

Fig. 10. Environmental records in the northern Lindos Bay section (left panel) and comparison with climate/environmental dynamics (right panel). Left panel (this study): foraminiferal data from the northern Lindos Bay section. Changes through time in the planktonic foraminiferal assemblages are shown with dashed horizontal lines (imported from Fig. 5) separating the clusters as inferred from the hCA performed on planktonic foraminiferal counts, with the estimated 7 «warmer» intervals in green and 7 «cooler» intervals in white. Environmental changes in the surface waters are also illustrated by the abundances of selected (sub)tropical (typified by *Globigerinoides ruber*) and temperate to subpolar (typified by *Neogloboquadrina pachyderma* and *Globorotalia inflata*) taxa (A), which are compared to the benthic (*Uvigerina peregrina*, black line) and planktonic (*Globigerina bulloides,* blue line) stable isotope ($\delta^{18}O_{VPDB}$ and $\delta^{13}C_{VPDB}$) records in the section (B) with the proposed identification of marine isotope stages between MIS 32 and MIS 21. (C) Paleodepths corrected from glacio-eustatic variations, with a LOESS regression (using PAST 3.22) of the estimated local paleodepth changes (red curve), the grey area representing the bootstrapped 95% confidence interval. Right panel (data from the literature): scheme of the chronology of

MIS succession (D) defined relative to the LR04 benthic global $\delta^{18}O$ stack of Lisiecki and Raymo (2005) with interglacials in grey. The Precession index and obliquity (E) are calculated based on the La04 (Laskar et al., 2004) astronomical solution, and the eastern Mediterranean sapropel record (F) is from ODP Sites 967 and 968 (Kroon et al., 1998; Konijnendijk et al., 2014).

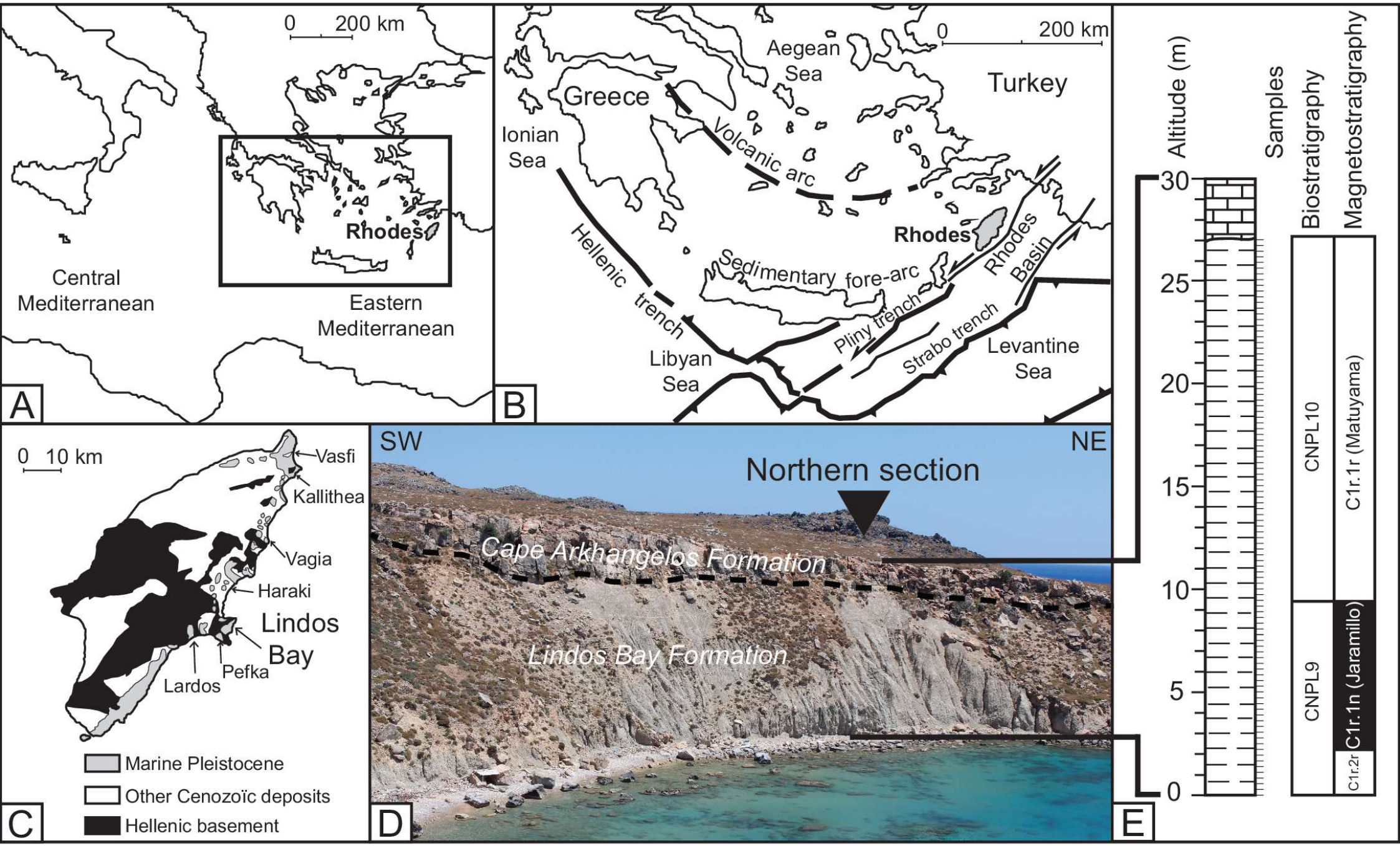

Quillévéré et al. - Figure 1 (two columns)

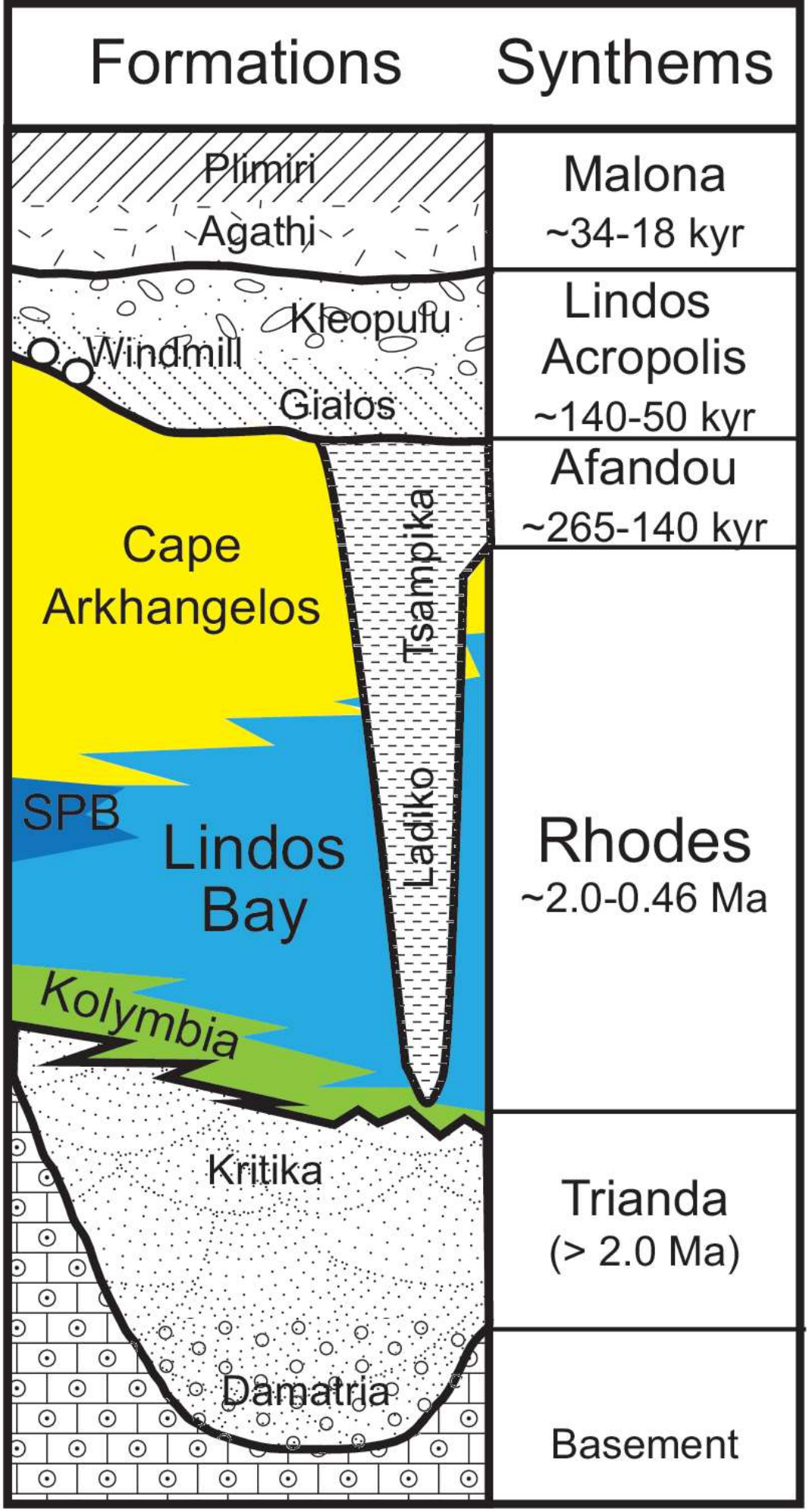

Quillévéré et al. - Figure 2 (single column)

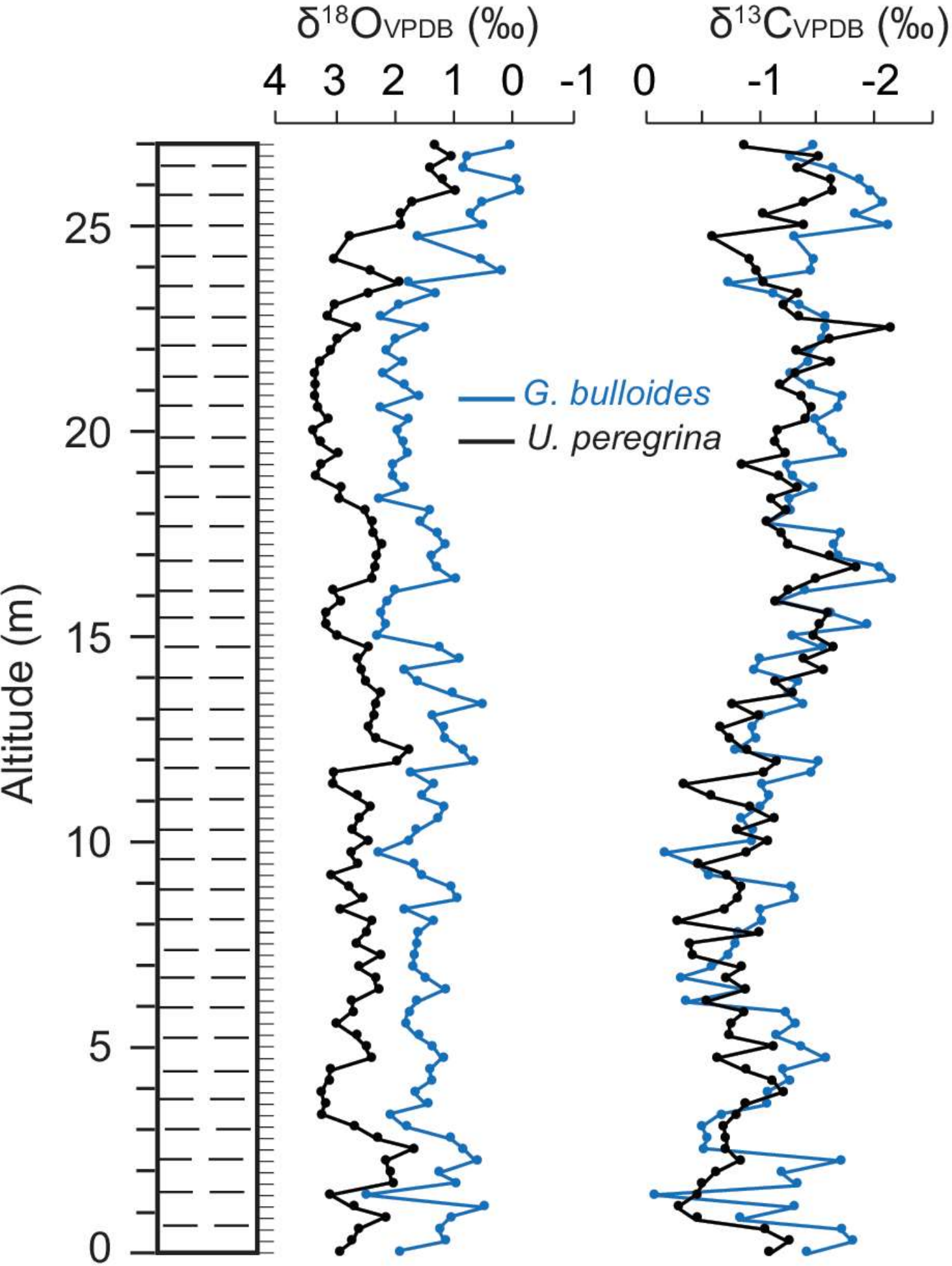

Quillévéré et al. - Figure 4 (single column)

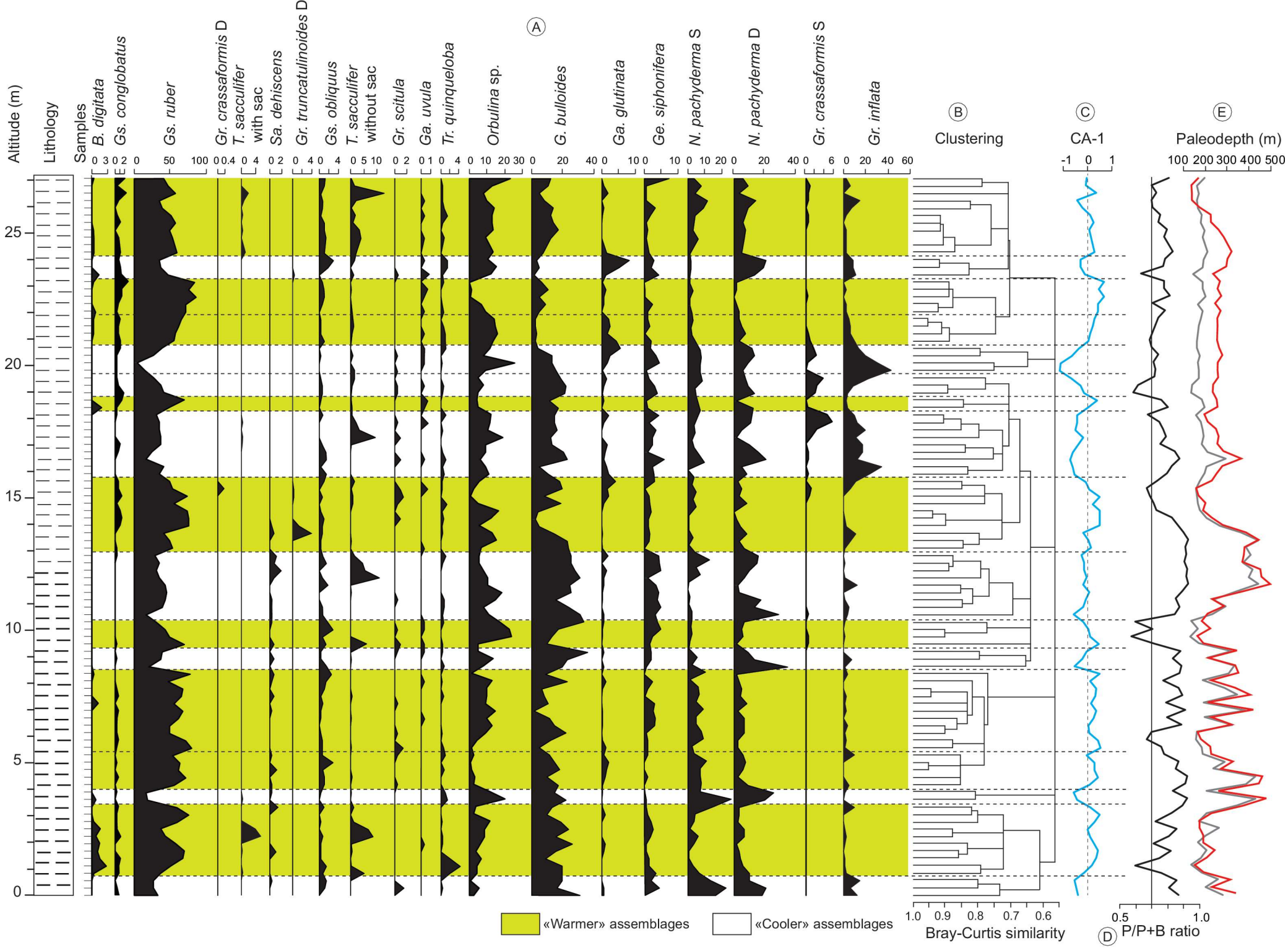

Quillévéré et al. - Figure 5 (two columns or full page)

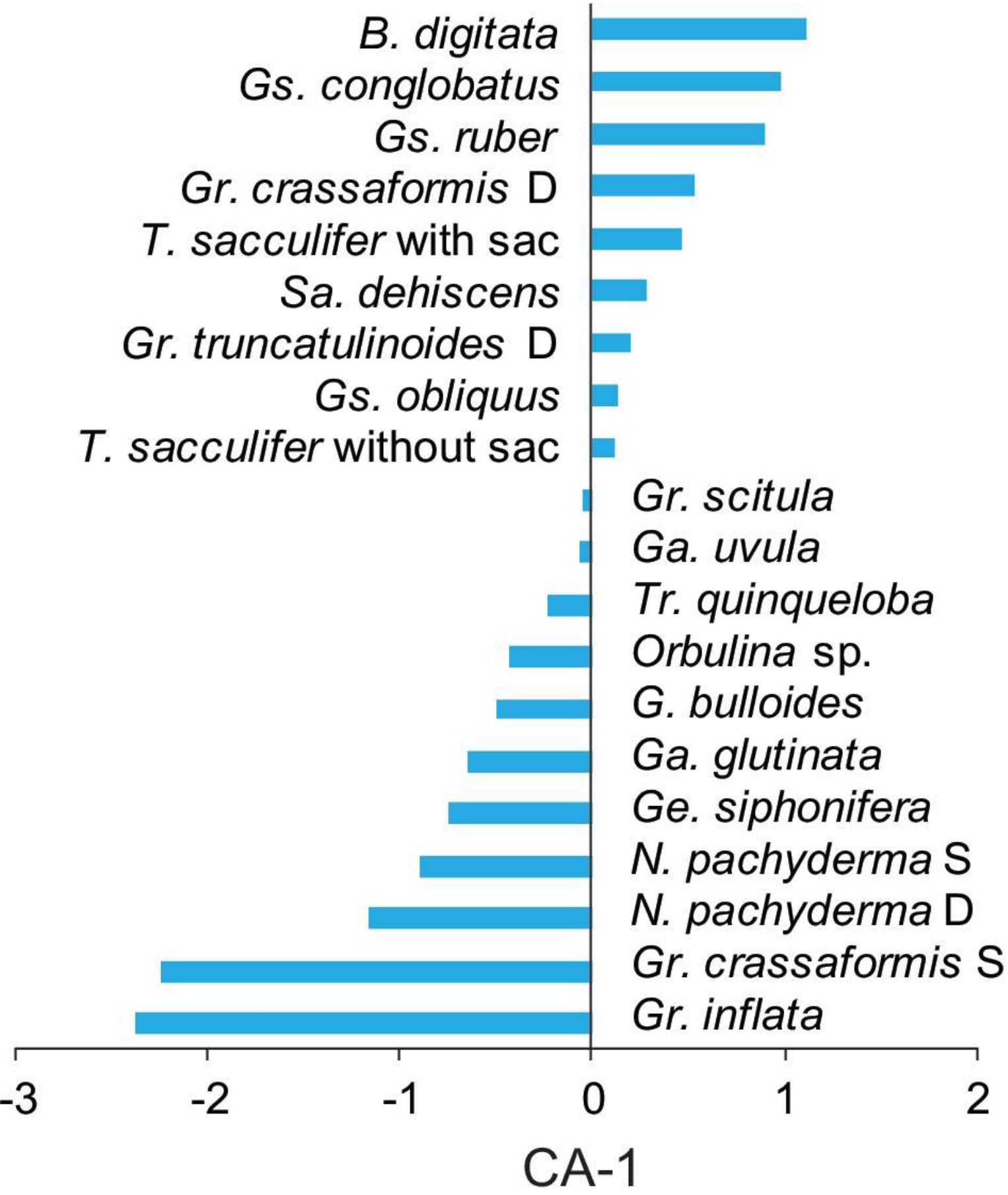

Quillévéré et al. - Figure 6 (single column)

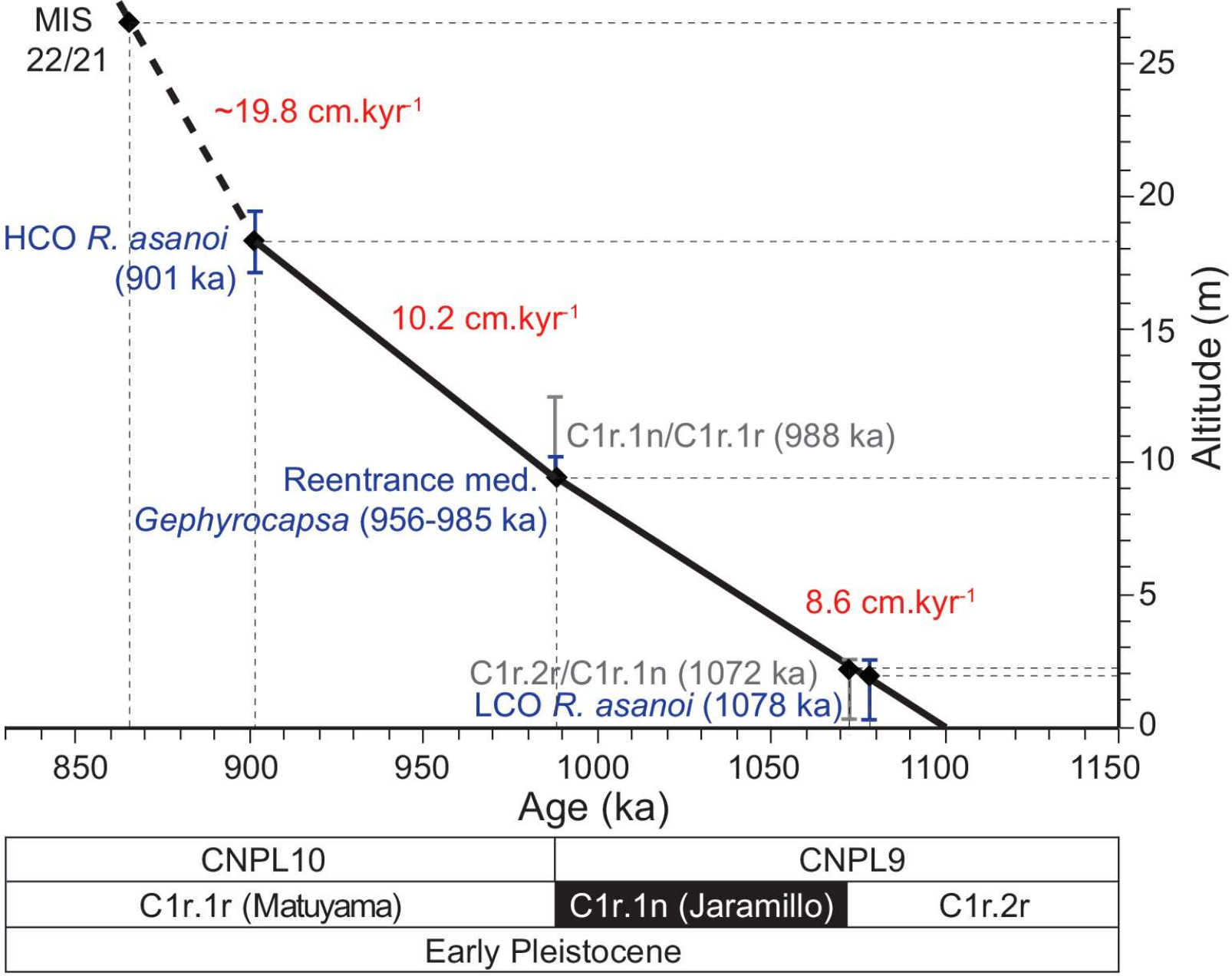

Quillévéré et al. - Figure 7 (single column)

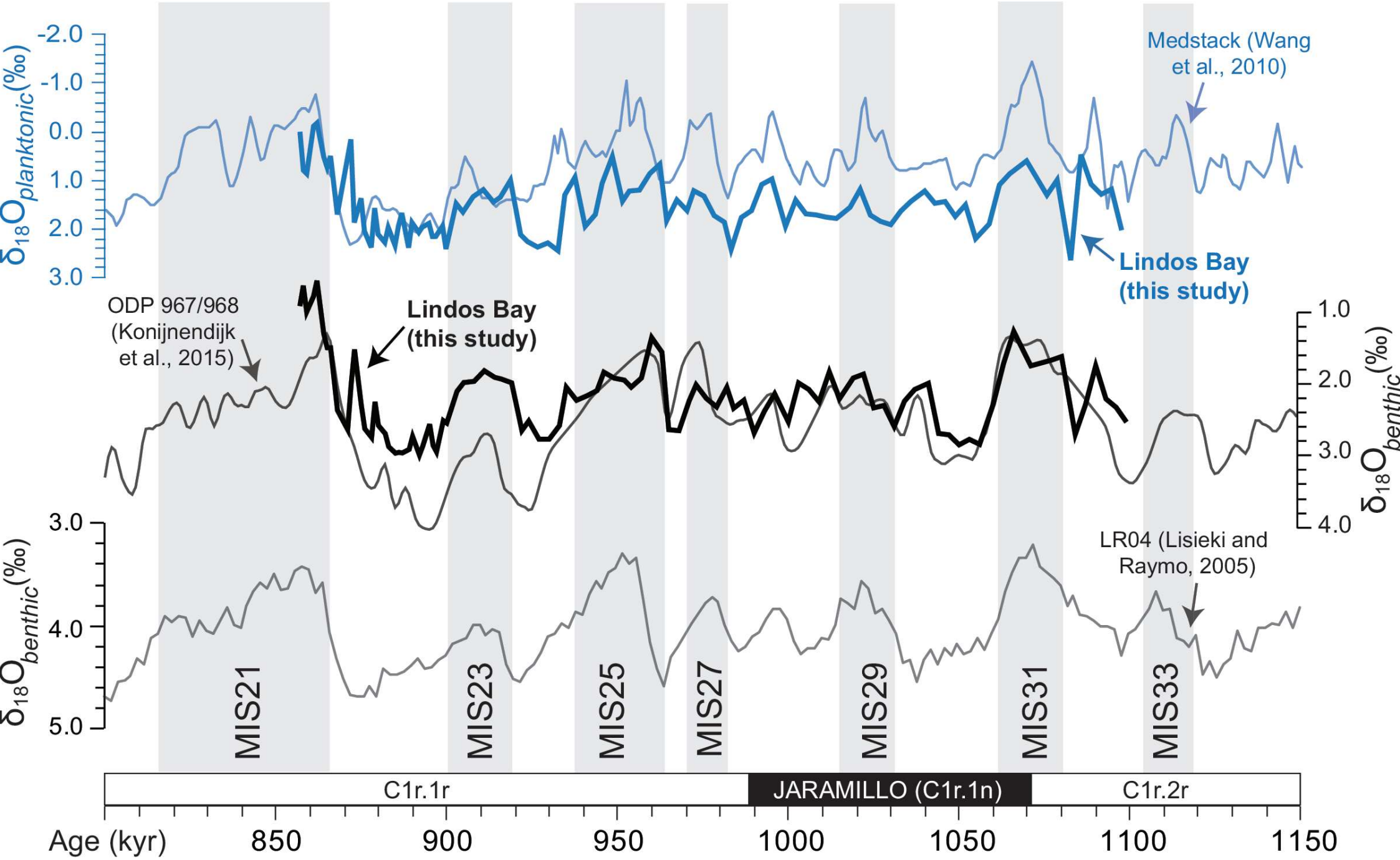

Quillévéré et al. - Figure 8 (two columns)

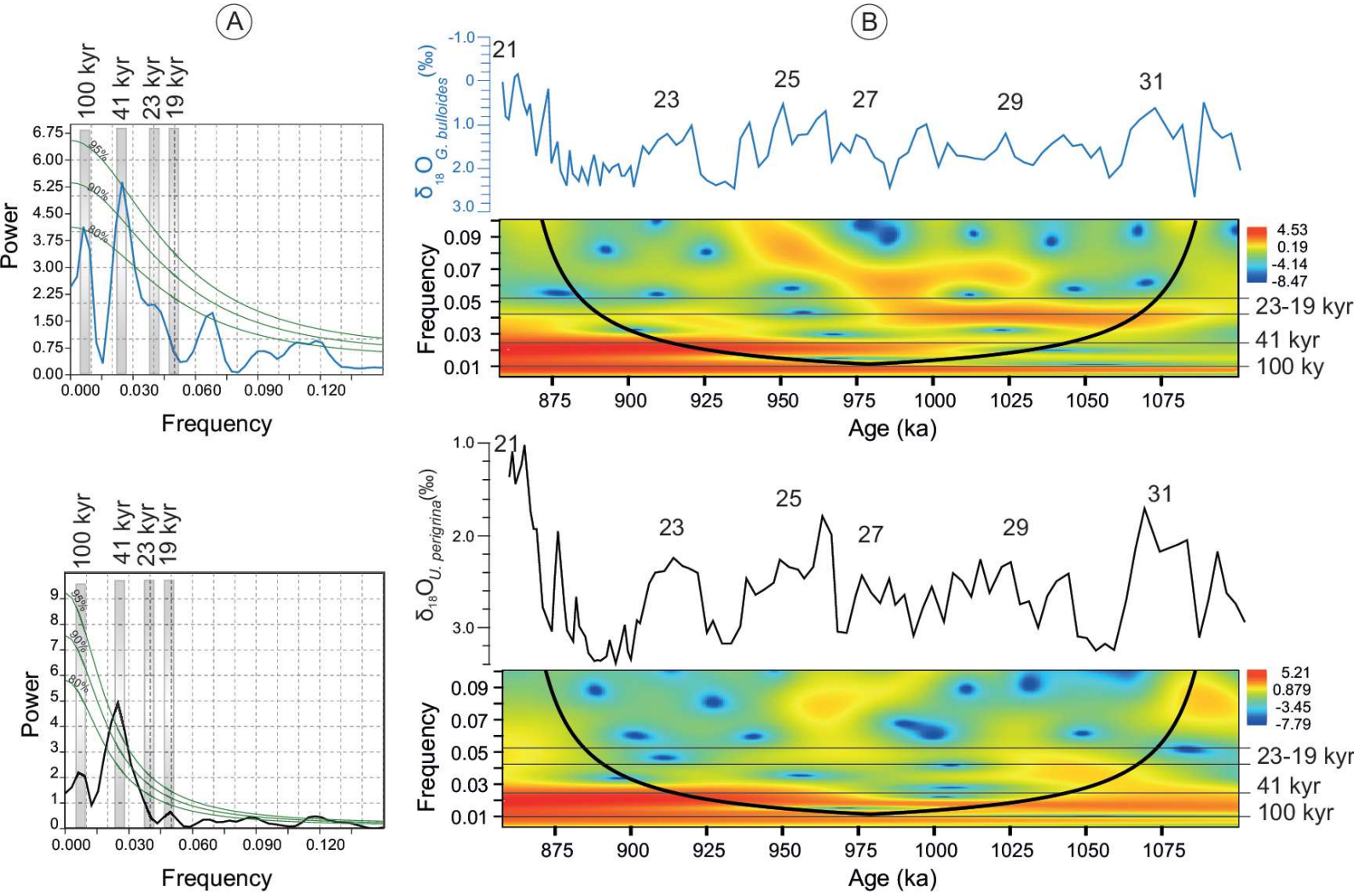

Quillévéré et al. - Figure 9 (two columns)

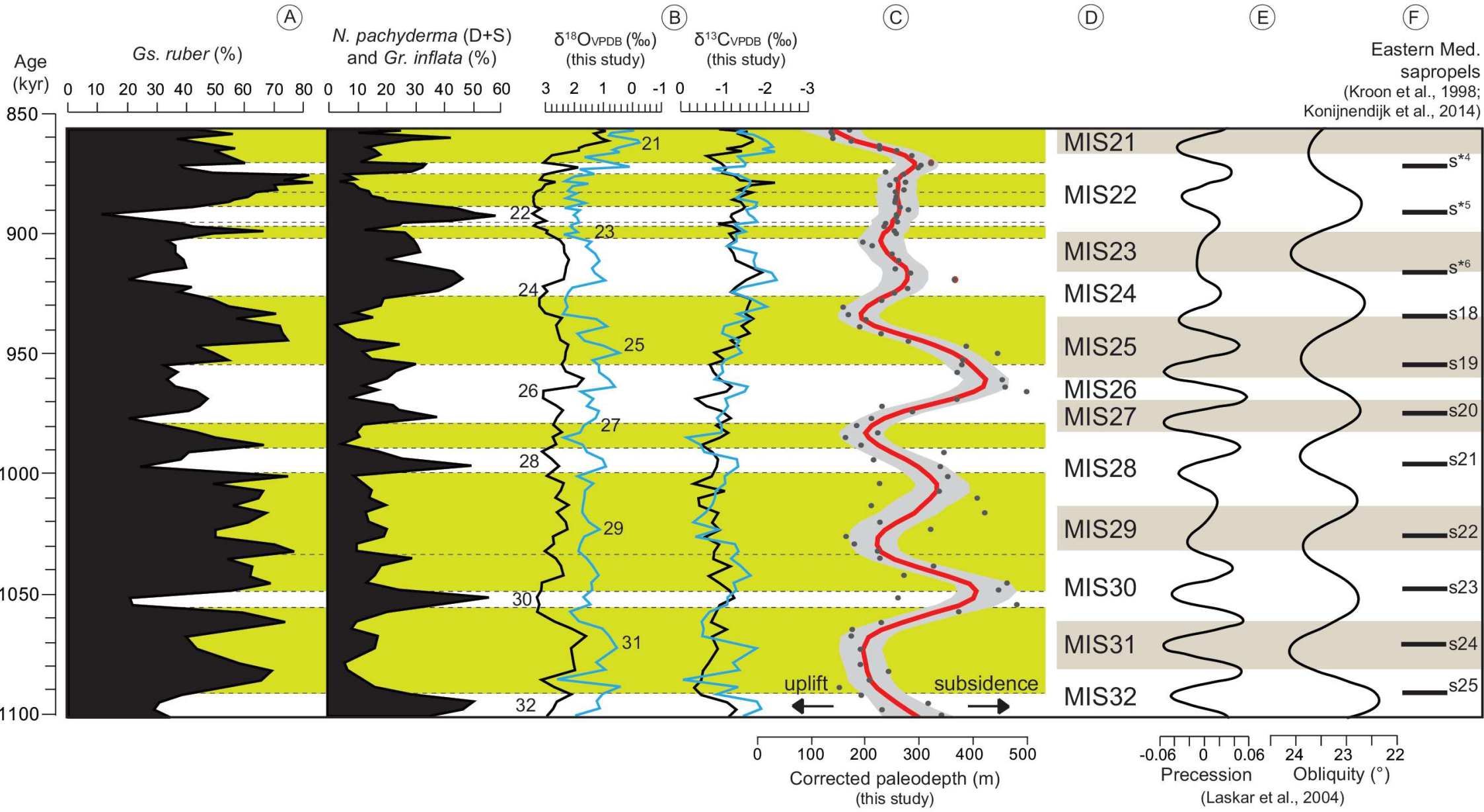

Quillévéré et al. - Figure 10 (two columns)

Table 1. Checklist of samples analyzed, age, stable isotope and paleodepth data

Sample	Altitude (cm)	Age (ka)	Taxa analyzed for stable isotopes	Number of specimens	Weight (µg)	$\delta^{18}O_{VPDB}$ (‰)	$\delta^{13}C_{VPDB}$ (‰)	P/P+B	Paleodepth (m)	Corrected paleodepth (m)**
LE98	2700	858	*G. bulloides*	10	125	0.064	-1.461	0.81	198	171
			U. peregrina	8	146	1.337	-0.859			
LE97	2672	859	*G. bulloides*	13	193	0.791	-1.259	0.70	162	138
			U. peregrina	10	139	1.057	-1.509			
LE96	2644	860	*G. bulloides*	18	123	0.856	-1.635	0.73	172	140
			U. peregrina	10	117	1.416	-1.324			
LE95	2616	862	*G. bulloides*	20	229	-0.042	-1.866	0.70	163	140
			U. peregrina	8	138	1.203	-1.616			
LE94	2589	863	*G. bulloides*	22	328	-0.100	-1.960	0.71	165	174
			U. peregrina	13	233	0.988	-1.629			
LE93	2561	865	*G. bulloides*	13	147	0.538	-2.069	0.76	181	226
			U. peregrina	14	310	1.719	-1.381			
LE92	2533	866	*G. bulloides*	15	128	0.735	-1.826	0.75	176	227
			U. peregrina	13	277	1.910	-1.024			
LE91	2505	867	*G. bulloides*	24	345	0.524	-2.115	0.80	195	261
			U. peregrina	11	180	1.911	-1.379			
LE90	2477	869	*G. bulloides*	15	199	1.626	-1.296	0.79	189	285
			U. peregrina	9	153	2.772	-0.581			
LE88	2422	872	*G. bulloides*	11	109	0.562	-1.466	0.84	208	321
			U. peregrina	14	149	3.037	-0.906			
LE87	2394	873	*G. bulloides*	7	87	0.209	-1.440	0.79	191	302
			U. peregrina	8	102	2.424	-0.966			
LE86	2366	874	*G. bulloides*	17	134	1.779	-0.720	0.78	187	297
			U. peregrina	10	142	1.936	-1.026			
LE85	2338	876	*G. bulloides*	7	98	1.323	-1.113	0.64	144	237
			U. peregrina	12	139	2.457	-1.329			
			*U. peregrina**	12	230	2.707	-0.942			
LE84	2310	877	*G. bulloides*	12	124	1.942	-1.342	0.78	188	268
			U. peregrina	12	207	3.026	-1.203			
LE83	2282	879	*G. bulloides*	26	314	2.249	-1.568	0.78	188	257
			U. peregrina	9	175	3.146	-1.337			
LE82	2255	880	*G. bulloides*	10	158	1.507	-1.567	0.82	202	274
			U. peregrina	9	145	2.657	-2.137			
LE81	2227	881	*G. bulloides*	15	188	2.000	-1.538	0.71	165	246
			U. peregrina	8	176	2.982	-1.605			
LE80	2199	883	*G. bulloides*	9	102	2.155	-1.422	0.79	190	271
			U. peregrina	10	186	3.094	-1.316			
LE79	2171	884	*G. bulloides*	12	150	1.873	-1.418	0.75	176	256
			U. peregrina	15	265	3.274	-1.614			
LE78	2143	886	*G. bulloides*	13	115	2.212	-1.263	0.73	170	257
			U. peregrina	17	264	3.363	-1.307			
LE77	2115	887	*G. bulloides*	13	135	1.848	-1.439	0.71	165	256
			U. peregrina	12	205	3.352	-1.172			
LE76	2088	888	*G. bulloides*	11	137	1.601	-1.716	0.69	159	255
			U. peregrina	11	178	3.360	-1.359			
LE75	2060	890	*G. bulloides*	17	187	2.254	-1.680	0.70	163	264
			U. peregrina	7	119	3.311	-1.447			
LE74	2032	891	*G. bulloides*	14	213	1.782	-1.478	0.74	175	279
			U. peregrina	9	158	3.133	-1.395			
LE73	2004	893	*G. bulloides*	20	288	1.966	-1.541	0.72	166	258
			U. peregrina	12	237	3.388	-1.151			
LE72	1976	894	*G. bulloides*	27	409	1.867	-1.627	0.73	170	257
			U. peregrina	9	146	3.263	-1.129			

LE71	1948	896	*G. bulloides*	19	353	1.796	-1.721	0.72	168	260
			U. peregrina	11	157	2.965	-1.220			
LE70	1921	897	*G. bulloides*	23	367	2.044	-1.233	0.62	139	237
			U. peregrina	11	160	3.256	-0.839			
LE69	1893	898	*G. bulloides*	19	269	2.043	-1.284	0.59	132	235
			U. peregrina	18	111	3.344	-1.163			
LE68	1865	900	*G. bulloides*	19	296	1.846	-1.463	0.77	183	253
			U. peregrina	9	179	2.915	-1.325			
LE67	1837	901	*G. bulloides*	16	249	2.279	-1.253	0.81	197	257
			U. peregrina	7	138	2.948	-1.096			
LE66	1809	904	*G. bulloides*	11	188	1.420	-1.265	0.68	156	197
			U. peregrina	15	234	2.511	-1.227			
LE65	1781	906	*G. bulloides*	8	133	1.582	-1.065	0.75	178	212
			U. peregrina	7	175	2.390	-1.056			
LE64	1754	909	*G. bulloides*	16	212	1.291	-1.701	0.78	186	250
			U. peregrina	9	195	2.374	-1.184			
LE63	1726	912	*G. bulloides*	19	232	1.158	-1.641	0.79	192	262
			U. peregrina	9	212	2.228	-1.242			
LE62	1698	915	*G. bulloides*	21	323	1.393	-1.682	0.76	181	256
			U. peregrina	8	149	2.318	-1.606			
LE61	1670	917	*G. bulloides*	29	309	1.302	-2.040	0.85	212	284
			U. peregrina	12	179	2.342	-1.837			
LE60	1642	920	*G. bulloides*	26	223	0.982	-2.148	0.88	294	365
			U. peregrina	9	152	2.394	-1.485			
LE59	1614	923	*G. bulloides*	16	231	2.011	-1.390	0.83	204	279
			U. peregrina	11	209	3.051	-1.246			
LE58	1587	925	*G. bulloides*	18	319	2.139	-1.168	0.80	195	254
			U. peregrina	9	170	2.921	-1.132			
LE57	1559	928	*G. bulloides*	18	251	2.244	-1.615	0.74	174	231
			U. peregrina	7	110	2.640	-2.233			
			*U. peregrina**	21	302	3.170	-1.589			
LE56	1531	931	*G. bulloides*	16	213	2.165	-1.932	0.68	155	160
			U. peregrina	9	155	3.170	-1.517			
LE55	1503	934	*G. bulloides*	13	118	2.311	-1.280	0.69	160	170
			U. peregrina	17	243	2.983	-1.464			
LE54	1475	936	*G. bulloides*	11	110	1.258	-1.546	0.71	166	202
			U. peregrina	12	157	2.455	-1.638			
LE53	1447	939	*G. bulloides*	11	107	0.923	-0.995	0.74	173	191
			U. peregrina	8	122	2.635	-1.378			
LE52	1420	942	*G. bulloides*	21	201	1.852	-0.946	0.83	206	230
			U. peregrina	16	209	2.564	-1.296			
			*U. peregrina**	13	245	2.574	-1.553			
LE51	1392	945	*G. bulloides*	15	253	1.627	-1.331	0.87	269	280
			U. peregrina	30	399	2.501	-1.132			
LE50	1364	947	*G. bulloides*	18	233	1.037	-1.247	0.91	367	386
			U. peregrina	13	192	2.248	-1.284			
LE49	1336	950	*G. bulloides*	19	218	0.531	-1.374	0.94	445	444
			U. peregrina	14	381	2.329	-0.756			
LE48	1308	953	*G. bulloides*	26	460	1.376	-1.011	0.91	388	380
			U. peregrina	7	154	2.357	-0.988			
LE47	1280	955	*G. bulloides*	20	291	1.184	-0.932	0.92	409	377
			U. peregrina	6	120	2.454	-0.651			
LE46	1253	958	*G. bulloides*	8	120	1.166	-0.964	0.91	374	370
			U. peregrina	6	111	2.328	-0.733			
LE45	1225	961	*G. bulloides*	12	176	0.857	-0.781	0.93	416	452
			U. peregrina	8	145	1.771	-0.884			
LE44	1197	964	*G. bulloides*	16	229	0.676	-1.507	0.92	402	457
			U. peregrina	7	110	1.972	-1.143			

LE43	1169	966	*G. bulloides*	26	465	1.744	-1.444	0.94	445	497
			U. peregrina	7	123	3.040	-1.030			
LE42	1141	969	*G. bulloides*	12	230	1.353	-1.016	0.90	340	369
			U. peregrina	8	133	3.053	-0.332			
LE41	1113	972	*G. bulloides*	13	162	1.553	-1.076	0.85	238	232
			U. peregrina	9	137	2.639	-0.571			
LE40	1086	974	*G. bulloides*	15	258	1.179	-0.100	0.88	294	287
			U. peregrina	10	185	2.422	-0.910			
LE39	1058	977	*G. bulloides*	25	422	1.281	-0.833	0.85	232	212
			U. peregrina	14	247	2.609	-1.124			
LE38	1030	980	*G. bulloides*	11	196	1.649	-0.936	0.60	135	185
			U. peregrina	10	173	2.726	-0.796			
LE37	1002	983	*G. bulloides*	10	161	2.450	-0.521	0.71	164	224
			*G. bulloides**	17	154	1.773	-0.927			
			U. peregrina	12	162	2.690	-0.894			
			*U. peregrina**	14	147	2.457	-1.066			
LE36	974	985	*G. bulloides*	13	175	2.288	-0.166	0.58	129	165
			U. peregrina	9	144	2.744	-0.879			
LE35	946	988	*G. bulloides*	13	212	1.684	-0.465	0.72	169	193
			U. peregrina	9	192	2.634	-0.457			
LE34	919	991	*G. bulloides*	20	317	1.554	-0.551	0.89	320	345
			U. peregrina	8	119	3.084	-0.708			
LE33	891	994	*G. bulloides*	23	328	1.060	-1.271	0.84	208	216
			U. peregrina	5	124	2.784	-0.834			
LE32	863	997	*G. bulloides*	26	374	0.957	-1.299	0.89	334	338
			U. peregrina	5	116	2.546	-0.803			
LE31	835	1001	*G. bulloides*	11	197	1.851	-0.100	0.88	307	352
			U. peregrina	8	137	2.931	-0.688			
LE30	807	1004	*G. bulloides*	21	436	1.356	-1.014	0.78	186	227
			U. peregrina	6	182	2.396	-0.278			
LE29	779	1007	*G. bulloides*	8	136	2.120	-0.609	0.87	288	336
			*G. bulloides**	16	190	1.616	-0.805			
			U. peregrina	10	247	2.371	-0.470			
			*U. peregrina**	11	100	2.485	-0.990			
LE28	752	1010	*G. bulloides*	10	132	1.635	-0.783	0.90	347	406
			U. peregrina	8	187	2.656	-0.386			
LE27	724	1013	*G. bulloides*	13	142	1.678	-0.721	0.80	193	212
			U. peregrina	8	222	2.244	-0.410			
LE26	696	1016	*G. bulloides*	8	158	1.702	-0.577	0.91	388	420
			U. peregrina	7	156	2.612	-0.838			
LE25	668	1020	*G. bulloides*	13	255	1.493	-0.308	0.80	195	228
			U. peregrina	9	212	2.328	-0.702			
LE24	640	1023	*G. bulloides*	23	338	1.151	-0.875	0.89	327	321
			U. peregrina	9	219	2.275	-0.871			
LE23	612	1026	*G. bulloides*	12	242	1.903	-0.174	0.70	163	166
			*G. bulloides**	13	287	1.640	-0.352			
			U. peregrina	9	257	2.816	-0.427			
			*U. peregrina**	12	312	2.739	-0.531			
LE22	585	1029	*G. bulloides*	20	304	1.758	-1.227	0.67	154	181
			U. peregrina	10	213	2.706	-0.859			
LE21	557	103	*G. bulloides*	14	270	1.820	-1.308	0.77	183	224

		2								
			U. peregrina	5	137	2.996	-0.748			
LE20	529	1035	*G. bulloides*	12	173	1.560	-1.140	0.78	187	228
			U. peregrina	8	209	2.647	-0.729			
LE19	501	1038	*G. bulloides*	21	307	1.377	-1.355	0.87	288	327
			U. peregrina	11	111	2.486	-1.116			
LE18	473	1042	*G. bulloides*	20	304	1.184	-1.573	0.85	238	272
			U. peregrina	6	190	2.401	-0.625			
LE17	445	1045	*G. bulloides*	18	281	1.416	-1.199	0.93	431	461
			U. peregrina	6	108	3.092	-0.877			
LE16	418	1048	*G. bulloides*	18	360	1.383	-1.260	0.91	388	445
			U. peregrina	10	189	3.110	-1.104			
LE15	390	1051	*G. bulloides*	22	357	1.664	-1.065	0.84	207	261
			U. peregrina	21	384	3.248	-1.204			
LE14	362	1054	*G. bulloides*	14	448	1.446	-1.059	0.93	431	479
			U. peregrina	24	335	3.173	-0.871			
LE13	334	1057	*G. bulloides*	28	616	2.083	-0.664	0.90	347	372
			U. peregrina	14	317	3.241	-0.792			
LE12	306	1061	*G. bulloides*	15	198	1.807	-0.492	0.83	205	229
			U. peregrina	12	330	2.689	-0.679			
LE11	278	1064	*G. bulloides*	16	252	1.538	-0.198	0.73	170	175
			*G. bulloides**	17	243	1.068	-0.537			
			U. peregrina	7	137	2.131	-1.031			
			*U. peregrina**	11	217	2.297	-0.697			
LE10	251	1067	*G. bulloides*	14	173	0.859	-0.507	0.86	263	175
			U. peregrina	8	150	1.686	-0.697			
LE9	223	1072	*G. bulloides*	26	246	0.614	-1.707	0.81	199	192
			U. peregrina	15	268	2.160	-0.829			
LE8	195	1078	*G. bulloides*	16	238	1.260	-1.187	0.71	166	192
			U. peregrina	10	212	2.082	-0.615			
LE7	167	1081	*G. bulloides*	16	231	0.975	-1.325	0.83	204	244
			U. peregrina	13	269	2.033	-0.492			
LE6	139	1085	*G. bulloides*	15	304	2.393	-0.072	0.75	178	208
			*G. bulloides**	13	117	2.491	-0.078			
			U. peregrina	19	391	2.867	-0.494			
			*U. peregrina**	11	247	3.105	-0.451			
LE5	111	1088	*G. bulloides*	15	258	0.497	-1.299	0.60	135	153
			U. peregrina	7	205	2.696	-0.289			
LE4	84	1091	*G. bulloides*	20	301	1.056	-0.825	0.77	182	193
			U. peregrina	10	240	2.159	-0.453			
LE3	56	1094	*G. bulloides*	22	259	1.246	-1.712	0.86	257	315
			U. peregrina	14	258	2.616	-1.042			
LE2	28	1097	*G. bulloides*	18	344	1.150	-1.809	0.81	199	231
			U. peregrina	10	222	2.733	-1.254			

			*U. peregrina**	10	167	2.715	-1.369			
LE1	5	110 0	*G. bulloides*	10	195	1.924	-1.407	0.87	282	341
			U. peregrina	10	171	2.935	-1.078			

*Replicate analyses. The number of specimens picked for stable isotope analyses and their weight are indicated
** Paleodepths are corrected from the effect of relative sea-level changes